Title

Quantitative analysis of metabolic fluxes in brown fat and skeletal muscle during thermogenesis.

Journal

Nature Metabolism, 5(7)

Authors

Park, Grace

Haley, John

Le, Johnny

et al.

Publication Date

2023-07-01

DOI

10.1038/s42255-023-00825-8

Peer reviewed

HHS Public Access

Author manuscript

Nat Metab. Author manuscript; available in PMC 2024 January 01.

Published in final edited form as:

Nat Metab. 2023 July ; 5(7): 1204–1220. doi:10.1038/s42255-023-00825-8.

Quantitative analysis of metabolic fluxes in brown fat and skeletal muscle during thermogenesis

Grace Park[1,*], **John A. Haley**[2,*], **Johnny Le**[1,*], **Su Myung Jung**[3,*], **Timothy P. Fitzgibbons**[4], **Ekaterina D. Korobkina**[2], **Huawei Li**[2], **Shelagh M. Fluharty**[2], **Qingbo Chen**[2], **Jessica B. Spinelli**[2], **Chinmay M. Trivedi**[4,5,6], **Cholsoon Jang**[1,#], **David A. Guertin**[2,#]

[1]Department of Biological Chemistry, University of California Irvine, Irvine, CA, USA.

[2]Program in Molecular Medicine, UMass Chan Medical School, Worcester, MA, USA.

[3]Department of Biological Sciences, Sungkyunkwan University, Suwon, South Korea.

[4]Division of Cardiovascular Medicine, Department of Medicine, UMass Chan Medical School, Worcester, MA, USA.

[5]Department of Molecular, Cell, and Cancer Biology, UMass Chan Medical School, Worcester, MA, USA.

[6]Li-Weibo Institute for Rare Diseases Research, UMass Chan Medical School, Worcester, MA, USA.

Abstract

Adaptive thermogenesis by brown adipose tissue (BAT) dissipates calories as heat, making it an attractive anti-obesity target. Yet how BAT contributes to circulating metabolite exchange remains unclear. Here, we quantified metabolite exchange in BAT and skeletal muscle by arteriovenous metabolomics during cold exposure in fed male mice. This identified unexpected metabolites consumed, released, and shared between organs. Quantitative analysis of tissue fluxes showed that glucose and lactate provide ~85% of carbon for adaptive thermogenesis and that cold and CL-316,243 trigger markedly divergent fuel utilization profiles. In cold adaptation, BAT also dramatically increases nitrogen uptake by net consuming amino acids, except glutamine. Isotope tracing and functional studies suggests glutamine catabolism concurrent with synthesis

[#]Corresponding: Cholsoon Jang (choljang@uci.edu), David A Guertin (david.guertin@umassmed.edu).
[*]These authors contributed equally to this work.

Author contributions: D.A.G and C.J. conceived the project and supervised the study. G.P. performed sample processing and LC-MS analysis for the AV experiments. J.A.H. performed most of the animal experiments, performed sample preparation, and the experiments and analysis related to glutamine synthetase activity including the ammonia tracing studies. J.L. performed sample processing and LC-MS analysis for the glucose and glutamine tracing experiments. S.M.J. helped develop the AV collection strategy and assisted in early animal experiments and performed animal experiments for glutamine tracing. T.P.F. performed doppler imaging and analysis. E.D.K. assisted with animal dissections for AV experiments and ammonia tracing and provided protein samples for tissue panel and adipogenesis panel. H.L. assisted with the glutamine and ammonia tracing experiments and animal colony management. S.M.F., and Q.C. assisted with AV experiments and ammonia tracing, and animal dissections for blood flow, respectively. J.B.S. for assistance with ammonia tracing experiments. C.M.T. for assistance with blood flow experiments. G.P., J.A.H., J.L., S.M.J., C.J., and D.A.G wrote the manuscript.

Data and materials availability: All data needed to evaluate the conclusions in the paper are present in the paper and/or the Extended Tables. R scripts to conduct bootstrapping to calculate the confidence interval of the difference between tissue and serum area under the curve are available on GitHub: https://github.com/johnnl15/Bootstrapping_AUC_NitrogenFL_BATLiverSerum

Competing interests: The authors declare no competing interests.

via glutamine synthetase, which avoids ammonia buildup and boosts fuel oxidation. These data underscore the ability of BAT to function as a glucose and amino acid sink and provide a quantitative and comprehensive landscape of BAT fuel utilization to guide translational studies.

Introduction

Brown adipose tissue (BAT) is the site of non-shivering thermogenesis (NST), a mammalian homeostatic mechanism of expending energy derived from nutrient catabolism as heat [1]. BAT thermogenesis is stimulated by cold, pharmacological beta-adrenergic agonists or prolonged consumption of certain high calorie diets [1–7] and is mediated by Uncoupling Protein 1 (UCP1), an inner mitochondrial membrane protein that dissipates the electrochemical proton gradient as heat [1]. Muscle shivering also helps maintain euthermia during acute cold exposure, but shivering subsides with prolonged cold exposure during which adaptive NST by BAT predominates as the main defense of body temperature [8].

The presence of BAT in adult humans, confirmed over a decade ago [9–13], intensified interest in therapeutically stimulating adipocyte thermogenesis to combat obesity and fatty liver disease by functioning as a catabolic sink [14,15]. Recent studies indicate active BAT may also restrict tumor growth by competing for glucose[16]. Naturally, interest in understanding how BAT utilizes circulating fuels to support thermogenesis has grown in parallel [17–20]. However, quantitative details about which circulating metabolites are consumed or released by BAT remain unclear. Conventional -omics studies do not provide this information as they measure metabolic snapshots rather than dynamic metabolite exchange.

In the 1970s, landmark experiments in rats measuring regional blood flow and arterio-venous (AV) differences in oxygen concentrations established BAT as the main site of adaptive thermogenesis [21–25]. Recent advances in high-sensitivity liquid chromatography-mass spectrometry (LC-MS)-based metabolomics is renewing interest in AV sampling to quantify organ-specific metabolite exchange [26–28]. The goal of this study was to adapt AV metabolomics for quantifying net BAT and skeletal muscle metabolic fluxes in different thermogenic states. Although larger organisms (rats, pigs, humans) are more amenable to this technique, we miniaturized AV sampling for mice because they are the most widely used model for studying metabolic diseases, are genetically manipulatable, and because pigs lack conventional BAT (i.e. they lack UCP1) [29,30].

Our results indicate that glucose and lactate predominate as BAT fuel sources in ad libitum fed male mice across all conditions tested here, that a commonly used pharmacological cold mimetic (CL316,243) shows different metabolic fluxes from physiological cold, that metabolite exchange between BAT and muscle varies with the mode and duration of thermogenesis, and that BAT is an avid consumer of amino acids but may upregulate glutamine synthesis to manage toxic nitrogen accumulation. These and additional findings herein establish a foundational and comprehensive landscape for understanding nutrient fluxes during thermogenesis in vivo.

Results

Establishing AV metabolomics in mice

To quantify tissue-specific metabolic flux during thermogenesis, we established an AV metabolomics method for BAT and skeletal muscle using mice (See Methods). Briefly, systemic arterial blood is collected from the left ventricle while BAT and leg-draining venous blood are collected from the Sulzer's and femoral vein, respectively (Extended Data Fig. 1a). Then, the metabolite's net uptake and release by BAT and leg are determined from the AV gradients of individual metabolites. Higher metabolite abundance in arterial than venous blood reflects net absorption, lower abundance reflects net release, and no difference reflects either no activity (bypass) or equal absorption and release (net zero exchange) (Extended Data Fig. 1b).

To validate our AV sampling method, we compared the abundance of 659 circulating metabolites between each blood sample collected from mice given free access to a standard chow diet (60% carbohydrate, 26% protein, 14% fat) and living at the standard vivarium temperature (22°C, which is mild cold for mice) or acutely cold exposed (6°C). These data reveal distinct circulating metabolome signatures between arterial blood and blood from the Sulzer's vein (BAT) or femoral vein (leg). Importantly, we identified metabolites that change abundance at different temperatures in a tissue-specific manner (Extended Data Fig. 1c).

We next established four unique cohorts of male mice: (a) thermoneutral adapted (30°C for 4 weeks, TN), (b) chronic cold-adapted (stepwise drop from 30°C to 6°C, over a 4 week period, CC), (c) thermoneutral adapted followed by acute cold exposure (direct drop from 30°C to 6°C for 4 hours, AC), and (d) thermoneutral adapted followed by acute CL316,243 treatment (30°C plus CL316,243 for 4 hours, CL), all fed ad libitum (Fig. 1a). AV blood sampling and metabolite quantitation by LC-MS was then performed on each cohort. BAT tissue was also collected to confirm UCP1 protein induction by Western blot and tissue remodeling by H&E stain. We noted that while CC adapted mice eat more, they had lower body weights compared to matched TN mice after 4 weeks (Extended Data Fig. 2a–b) consistent with a higher metabolic rate in cold. There were no changes in total body weight during 4-hour exposure to AC or CL (Extended Data Fig. 2b). CC robustly increases UCP1 and greatly reduces lipid droplet size; in contrast, AC and CL only mildly induce UCP1 and moderately decrease lipid droplet size (Extended Data Fig. 2c–d). This suggests that the demand for nutrient uptake from circulation (i.e. the ability to function as a catabolic sink) is greater upon cold adaptation when intracellular stored fuel is more depleted.

Cold adaptation promotes BAT uptake of diverse metabolites

Using thermoneutral (TN) as the benchmark, we first examined how BAT's metabolite uptake and release change upon cold adaptation (CC), a condition in which euthermia is primarily maintained by NST. By calculating $\log_2$ ratios of venous to arterial blood concentration, we quantitated the fractional uptake and release of each circulating metabolite. After cold adaptation, the number of metabolites absorbed by BAT nearly doubles (from 85 to 162), reflecting increased metabolic demand (Fig. 1b and Extended Table 1). Notable absorbed metabolites include medium and long-chain non-esterified fatty

acids (MCFA, LCFA), consistent with their roles as thermogenic fuel. However, the uptake of six indole derivatives was unexpected (Fig. 1b). These indoles are made by microbial tryptophan breakdown and may stimulate adipose differentiation [31], which has intriguing implications for BAT recruitment during chronic cold exposure. Interestingly, the purine nucleosides adenosine and guanosine are uniquely released in TN (Fig. 1b). Given that adenosine is reportedly an autocrine signaling metabolite that stimulates NST [32,33], the lack of release in CC may reflect trapping of these nucleoside ligands by their membrane GPCR receptors.

Next, we focused on 35 abundant and high flux-carrying circulating metabolites that are known building blocks and energy sources [34] (Fig. 1c–k). We used two independent statistical analyses to identify (i) metabolites that show significant uptake or release in each condition (by one sample t-test with null hypothesis of no uptake or release) and (ii) metabolites that have significantly different uptake/release activities between the conditions (by Student's t-test or ANOVA). In CC, BAT net absorbs almost all the abundant fuel metabolites, including glucose, lactate, 3-hydroxybutyrate (3HB, a ketone body) and LCFAs (Fig. 1c,1d). Most amino acids are also net taken up in CC (Fig. 1e–i), including the branched-chain amino acids (BCAAs) [35,36]. Noteworthy exceptions are alanine and glutamine, which show net zero exchange (Fig. 1i), suggesting bypass or equal absorption and release. Alanine and glutamine are the most abundant circulating amino acids, which in addition to being substrates, can function as nitrogen carriers in peripheral tissues where they assimilate excess nitrogen (largely produced from amino acid oxidation) and deliver it to the liver. Accordingly, the observation that BAT net absorbs many amino acids predicts a substantial release of nitrogen, for example as alanine and/or glutamine, to balance nitrogen levels; thus, their net zero exchange favors an equivalent uptake and release model (discussed below). Other abundant blood metabolites including TCA cycle intermediates, betaine, taurine, and creatine show no significant AV differences between TN and CC (Fig. 1j,1k). These AV ratio data show relative uptake and release but do not reflect absolute blood metabolite concentrations. For example, glucose shows a similar AV ratio as BCAAs (Fig. 1c and 1e); however, glucose uptake quantitatively contributes more carbon to the tissue because the blood glucose concentration is much higher than that of BCAAs. Extended Fig. 3 shows the absolute AV concentration gradient values (μM) for the indicated metabolites.

CL316,243 and acute cold differentially affect BAT

In addition to cold adaptation, acute cold exposure (AC) and CL316,243 administration (CL) are commonly used to assess thermogenesis. AC is also associated with muscle shivering, which subsides upon cold adaptation. Therefore, keeping TN as the benchmark, we next asked how AC and CL affect BAT metabolite uptake and release (Fig. 2a). Unlike cold adaptation (Fig. 1b), AC for 4 hours only slightly increases the number of metabolites that BAT absorbs (from 85 to 95) when compared to TN (Fig. 2a). This may reflect the fact that BAT relies more on its stored lipids and glycogen during the initial emergency response to cold exposure, while increasing glucose uptake and *de novo* lipid synthesis in CC (Extended Data Fig. 2c, 2d) [37,38]. In surprising contrast, acute CL treatment for the same duration (4 hours) dramatically increases the number of metabolites absorbed (from 85 to 209) (Fig. 1b, 2a and Extended Table 1). AC and CL also induce the release of distinct metabolites.

For example, BAT in AC specifically releases LCFAs while upon CL treatment, BAT net releases not only LCFAs but also MCFAs and very long-chain fatty acids (VLCFAs) (Fig. 2a). This may reflect higher lipolysis upon CL316,243 stimulation, as suggested by higher phosphorylation of BAT hormone-sensitive lipase (HSL) in the CL-treated mice (Extended Data Fig. 2c).

We also noted several unexpected differences between AC and CL. First, prostaglandin E1, pyrimidine, and xanthine are selectively released by BAT in AC (Fig. 2a), possibly as organ signaling metabolites [35,39–41]. For example, prostaglandin E1 may contribute to the vasodilation of BAT's proximal vasculature to facilitate circulating nutrient uptake[39]. Markedly distinct effects of AC and CL are also evident in the 35 high turn-over circulating fuels (Fig. 2b–j). Relative to TN, only acute CL (but not AC) significantly enhances net glucose uptake (Fig. 2b). While AC suppresses net release of LCFAs, CL slightly enhances it (Fig. 2c) and strongly increases the net uptake of several amino acids (Fig. 2d–h). Notably, even alanine and glutamine, which show net zero exchange in CC (Fig. 1i) are net absorbed upon CL injection (Fig. 2h), suggesting alternative nitrogen removal mechanisms such as protein synthesis or ammonia release. However, TCA cycle metabolites or other abundant metabolites do not show such enhanced uptake by CL (Fig. 2i, 2j). Thus, despite acute CL mimicking molecular features of acute cold exposure, such as moderate UCP1 induction and partial lipid depletion [1], it induces disparate BAT metabolite exchange compared to natural cold.

The landscape of metabolite exchange in thermogenic muscle

Acute cold exposure (AC), but not cold adaptation (CC), associates with muscle shivering [1]. Very little is known about circulating nutrient utilization by shivering muscle. Thus, we used AV metabolomics in legs, to systematically map the metabolite exchange of the leg in each condition (Extended Table 1). Intriguingly, all thermogenic states (CC, AC, and CL), regardless of muscle shivering, induce the release of carnosine and anserine (Fig. 3a–d), which are histidine di-peptides with reported signaling functions [42]. Carnosine supplementation induces white adipose tissue browning in rats [43] and mitigates high-fat diet-induced metabolic disorders [44]. Thus, muscle-derived anserine and carnosine may contribute to the systemic response to BAT stimulation.

Another unexpected observation is the release of creatine only in acute thermogenic conditions (AC and CL) (Fig. 3c, 3d). Under acute energic stress, conversion of phosphocreatine to creatine by the creatine kinase rapidly regenerates ATP from ADP via a phosphate transfer reaction. Thus, the release of creatine by legs in acute settings may reflect increased creatine kinase activity to buffer the abrupt increase in energy demand during emergency thermogenesis.

We next compared the leg uptake and release of the 35 primary fuel sources across the four conditions. Compared to TN, only CL induces net glucose uptake (Fig. 3e). Interestingly, neither glucose nor lactate are net consumed in CC, which may reflect the waning of shivering upon cold adaptation [1]. In contrast, legs take up 3-hydroxybutyrate across all four conditions and this is unchanged by any thermogenic state. CL but not AC induces pyruvate release, further highlighting differential metabolic impacts of these two conditions.

Curiously, LCFAs are overall released across the conditions (Fig. 3f), possibly reflecting femoral subcutaneous fat mobilization draining into the femoral vein.

Amino acid exchange by legs also shows distinct patterns between the conditions (Fig. 3g–3k). BCAAs are the most avidly and consistently net absorbed (Fig. 3h). BCAAs are particularly abundant in muscle proteins constituting about ~30% of the total amino acid content [45], suggesting their uptake may be for muscle protein synthesis and is independent of thermogenesis. Interestingly, glycine and serine, one-carbon pathway amino acids, are net absorbed in response to CC (Fig. 3j). Glycine reportedly protects against muscle wasting and oxidative stress [46,47]. We also observed evidence of inter-organ exchange between leg and BAT. For example, following CL treatment, glutamate is net released by leg (Fig. 3k) and net consumed by BAT (Fig. 2h); alanine shows a similar trend. Among the TCA cycle intermediates, succinate is net consumed by leg in CC or CL (Fig. 3l) while it is released from BAT (Fig. 1j, 2i). Other metabolites also exhibit different exchange patterns across the conditions (Fig. 3m).

Quantitative analyses of BAT carbon fluxes

We next used AV metabolite concentration gradients and blood flow to quantitatively assess the contribution of circulating metabolites to BAT total carbon flux (F_c):

$$Fc = Q(Cv - Ca)$$

where Q indicates BAT blood flow rate, measured by color and pulsed wave doppler ultrasound, and C_v and C_a indicate blood concentrations of carbon carried by each metabolite in the Sulzer's venous blood and arterial blood, respectively. This analysis revealed that under these conditions, CC substantially increases total BAT carbon influx compared to TN (from 235.7 to 1335 nmol C/s g BAT) (Fig. 4). The primary contributor to this increase is circulating glucose (~70% of carbon influx) (Fig. 4 and Extended Table 2). Circulating lactate and amino acids are the next major carbon contributors, providing ~15% and ~8% to BAT carbon influx, respectively (Fig. 4 and Extended Table 2). Despite such profound increases in nutrient consumption observed in CC versus TN, these values may *underestimate* net flux in the cold conditions (see methods). In contrast to CC, AC shows only slightly increased carbon influx compared to TN, consistent with BAT mainly relying on internal stored fuels and shivering in acute cold.

BAT can also use circulating lipids from triglyceride-rich lipoprotein particles such as chylomicrons and very-low-density lipoprotein (VLDL) [1,48–53]. Thus, we measured AV gradients of saponified circulating fatty acids that summate fatty acids from both albumin-bound non-esterified fatty acids and lipoprotein particles. From the total fatty acid pools, we then subtracted non-esterified fatty acids (measured separately without saponification) to calculate the contribution of lipids from lipoprotein particles. By this measure, we observe a net influx of lipoprotein fatty acid carbons in TN that accounts for ~20% of the total carbon influx (Fig. 4 and Extended Table 2). This contribution is largely maintained in AC, which aligns with previous reports that BAT uses circulating lipoprotein-derived fatty acids upon acute cold exposure [49,50]. While the contribution of lipoprotein lipid influx drops to 5% in

CC, the flux remains quantitively similar between TN and CC (~50 C nmol/s g BAT). We also observed a minor carbon influx from circulating acylcarnitines[54]. Overall, this supports a model in which BAT meets its energy demands in cold adaptation mainly by increasing glucose flux.

Our study was performed in *ad libitum* fed male mice with standard chow diet. In another study using similar conditions, thermogenic BAT also showed minimal uptake of circulating fatty acids [55]. In the fasted state, circulating lipid contribution is likely higher. In fact, a recent comprehensive fluxomics study using mice living in a mild cold (room temperature) environment support these observations, showing that BAT in a fed state prefers glucose while fatty acids become more important in a fasted state [17]. Quantitative differences in the use of circulating glucose vs. lipids may also show circadian dependencies particularly in cold adapted mice[56]. Despite carbon uptake from fatty acids being less substantial than glucose in our experiments, fatty acids may still act as signaling molecules [57].

Our findings support a model in which a significant fraction of the fatty acids oxidized by BAT are first synthesized *de novo* from other precursors such as glucose [21,38,58–60]. Additional fatty acids may diffuse from adjacent white adipose tissue especially during acute cold exposure when these depots are loaded with stored lipids; such local contribution is not captured by AV measurements. In the emergency state of acute cold, intracellular lipid droplets also provide fatty acid fuel, but in cold-adapted mice, the intracellular lipid droplets are greatly depleted of stored fuel (Extended Data Fig. 2d). The depletion of intracellular and local sources of lipid may be coordinated with the increase in *de novo* lipogenesis during the adaptive process, the advantage of which remains unknown.

In terms of carbon efflux, CC-adapted BAT releases succinate, but no other TCA cycle intermediate (Fig. 1j and Fig. 4). The selective net release of succinate may relate to succinate's unique adrenergic-independent accumulation in BAT and its role in generating reactive oxygen species [61]. Alternatively, certain cells in BAT may export succinate in response to hypoxia [62], given that BAT extracts nearly all oxygen from blood [63–65].

Quantitative analysis of BAT nitrogen fluxes

Next, we examined BAT nitrogen handling, which is a fundamental yet less appreciated aspect of BAT metabolism. In TN, total BAT nitrogen influx and efflux are relatively balanced (2.171 vs. 1.227 nmol N/s g BAT) (Fig. 5). Strikingly, however, total nitrogen influx increases in CC by ~12-fold (from 2.171 to 25.91 nmol N/s g BAT) while in contrast, total nitrogen efflux decreases by ~11-fold (from 1.227 to 0.1122 nmol N/s g BAT). This creates a considerable imbalance in nitrogen flux that is mainly driven by increased amino acid uptake in CC (Fig. 5 and Extended Table 3). While AC also increases nitrogen influx via amino acid uptake, the imbalance between influx and efflux is less significant. In the liver, excess nitrogen can be excreted in the form of urea, and production of some urea cycle metabolites have been reported in BAT [38,66–68]. However, we did not detect any significant release of urea or urea cycle intermediates by BAT (Extended Table 1), arguing against the possibility that urea cycle metabolites remove excess nitrogen from BAT. Alternatively, BAT may release ammonia [67] or incorporate the nitrogen into new protein synthesis. Consistent with the later, mTORC1, a main driver of protein synthesis, increases activity in BAT during

cold adaptation [69]. Moreover, the release of many proteins by thermogenic BAT has been reported (e.g., batokines) [18,70,71]. This is an important area for future investigation.

In terms of nitrogen efflux, BAT in TN and AC release nitrogen in the form of nucleosides (inosine, adenosine, thymidine, cytosine), bases (xanthine, hypoxanthine, adenine) and nucleotides (GMP, AMP, IMP) (Fig. 5), however, these metabolites are largely taken up by BAT in CC. For adenosine and inosine, this difference may be linked to their reported roles in stimulating thermogenic adipocyte differentiation and function[32,72,73]. These data suggest that BAT uses distinct nitrogen-rich metabolites as carriers depending upon the thermogenic state.

Different effects of CL316,243 and acute cold on BAT flux

We also examined the effects of acute CL316,243 on net tissue carbon and nitrogen flux. This revealed that, compared to TN, CL increases carbon influx by ~5.5-fold, respectively (Extended Data Fig. 4), which is higher than AC (Fig. 4). In terms of carbon efflux, CL treatment markedly increases it to a greater extent than other conditions, and this is primarily driven via the release of fatty acids (lipolysis), acylcarnitine (fat oxidation) and succinate (anaplerotic stress) (Fig. 4 and Extended Data Fig. 4). Regarding CL-induced changes in nitrogen flux, amino acid uptake dramatically increases total nitrogen influx (Extended Data Fig. 4), which is distinct from AC (Fig. 4). These data are consistent with CL316,243 differentially affecting BAT nutrient fluxes compared to cold conditions.

BAT both catabolizes and synthesizes glutamine during cold

Glutamine, the most abundant circulating amino acid, can be an important TCA cycle fuel in times of high energy demand. Thus, it was unexpected that glutamine shows a unique net zero exchange in CC (Fig 1i). Using stable isotope tracing of ^{13}C-glucose, we recently reported active glutamine synthesis from glucose by BAT in CC [38]. These data suggested that BAT may release and take up glutamine at similar rates, resulting in net zero exchange.

To investigate this hypothesis, we employed stable isotope tracing of [U-^{15}N,^{13}C]-glutamine to understand its catabolism and synthesis in the BAT of temperature challenged mice. Like in our previous glucose tracing study [38], mice were adapted to TN (30°C), mild cold (MC, 22°C) or severe cold (CC, 6°C) for 4 weeks. [U-^{15}N,^{13}C]-glutamine was then given intravenously, and BAT, liver and serum were harvested at 2.5-, 5- and 15-minutes post-delivery to capture the early events of glutamine usage by organs (Fig. 6a). We achieved 15–25% BAT enrichment of glutamine across conditions ([5+2] in Extended Data Fig. 5a). Compared to TN or MC, CC-adapted BAT markedly increases glutamine carbon contribution to the TCA cycle up to 20–30% (Extended Data Fig. 5b–c), which may be used for energy production and/or biosynthesis reactions (e.g., lipogenesis). To the latter point, CC-adapted BAT also shows higher M+5 citrate labeling compared to TN and MC (Extended Data Fig. 5d), which may reflect reverse TCA cycle flux (i.e., reductive carboxylation) for fatty acid synthesis (Extended Data Fig. 5e) [74–76]. This notion is consistent with highly upregulated *de novo* lipogenesis enzyme expression and flux in CC-adapted BAT (Extended Data Fig. 2c) [21,38,58,59,77–79]. In contrast to BAT, liver glutamine carbon entry into the TCA cycle overall decreases in MC or CC relative to TN (Extended

Data Fig. 5b, 5d), indicating that glutamine catabolism is shifting away from liver and towards BAT during the process of adapting to decreasing temperatures.

Rapid BAT transamination during cold adaptation

The nitrogen of glutamine is also more actively used by BAT in CC (Extended Data Fig. 6a). For example, CC BAT rapidly converts [U-^{15}N,^{13}C]-glutamine tracer to other forms of glutamine with different combinations of nitrogen and carbon labeled (^{15}N1/2-Gln isotopomers) (Fig. 6b, 6c, Extended Data Fig. 6b), consistent with *de novo* glutamine synthesis. Circulating glutamate can be a precursor because BAT actively takes up glutamate in CC (Fig. 1i) and in activated human BAT [80]. At the same time, CC BAT shows higher ^{15}N-labeled alanine and aspartate, the two major amino acids made via trans-amination reaction from pyruvate and oxaloacetate (Fig. 6b–6e). Several other amino acids also show increased incorporation of ^{15}N in CC (Fig. 6f, 6g). Together, these data indicate an instantaneous exchange of labeled nitrogen between glutamine and other amino acids in CC BAT (Extended Data Fig. 6b). Interestingly, this phenomenon is largely suppressed or unaffected by temperature in the liver (Fig. 6h–6m), indicating that it is BAT-specific.

Some of the ^{15}N-labeled amino acids in BAT may be generated in other organs (e.g., liver) and subsequently taken up by BAT (Fig. 6n). To identify such inter-organ exchange, we compared fractional labeling of each metabolite in tissues relative to serum, based on the principle that the fractional labeling can only be decreased during metabolite transformation and trafficking (Fig. 6o). This analysis suggested that: a) both BAT and liver generate ^{15}N-glutamine and glutamate (Fig. 6p), b) other amino acids show organ-specific and temperature-sensitive transamination, i.e. BCAAs by BAT (Fig. 6q); asparagine, alanine and aromatic amino acids by liver (Fig. 6r), serine, glycine, proline, and aspartate potentially by BAT, liver or other organs (Fig. 6s), and c) circulating urea cycle metabolites are not mainly from BAT (Fig. 6t) despite their synthesis reported in cultured preadipocytes [66]. Additionally, ^{15}N-labeled alanine in BAT (Fig. 6b) may be produced by the liver and taken up by BAT (Fig. 6r), highlighting a crosstalk between BAT and liver.

BAT glutamine synthesis increases during cold adaptation

AV metabolomics and isotope tracing data suggest concurrent glutamine catabolism and synthesis in cold-adapted BAT. We wondered why this occurs and whether it is necessary for BAT thermogenesis. Glutamine synthesis is carried out by glutamine synthetase (GS), which is encoded by the *glutamine ammonia ligase* (*Glul*) gene. GS condenses ammonia onto glutamate to generate glutamine in an ATP-dependent reaction, while the breakdown of glutamine into glutamate is carried out by glutaminase (GLS) in the glutaminolysis pathway (Fig. 7a). Glutamine synthesis is known to occur in the brain, kidneys, liver, and skeletal muscle. In the brain, glutamine synthesis is critical for preventing toxic levels of ammonia from accumulating and to regulate neurotransmitter levels.

In BAT, the levels of *Glul* mRNA (Fig. 7b, Extended Data Fig. 7a) and its protein product GS (Fig. 7c) robustly increase after cold adaptation. In contrast, hepatic GS expression does not respond to cold (Fig. 7d). GS is also upregulated during brown adipocyte differentiation in vitro (Extended Data Fig. 7b). *In vivo*, under standard temperature (mild cold) and dietary

conditions, BAT GS protein expression is comparable to the high levels observed in liver and brain (Extended Data Fig. 7c). Notably, we did not see a matching increase in *Gls* mRNA or protein expression (Fig. 7b, 7c) despite the increased BAT glutamine catabolism (Extended Data Fig. 5a–d). This is consistent with the frequent mismatch between pathway flux and mRNA or protein expression.

To directly examine GS activity in BAT, we established an *in vivo* GS activity assay by performing ^{15}N-ammonia (^{15}N-NH_4Cl) tracing (Fig. 7e). In BAT from CC mice, nitrogen from ^{15}N-ammonia is rapidly assimilated into glutamine, reaching maximum fractional labeling (~40%) by 2.5 minutes (Fig. 7f, 7h). Glutamate labeling carried out by glutamate dehydrogenase 1 (GLUD1) was much lower (~2%) (Fig. 7h) but the fractional labelling is still higher in CC compared to the TN (Fig. 7g). This labeling difference between glutamine and glutamate indicates that ammonia assimilation mainly occurs directly onto glutamate via GS to make glutamine, rather than through the GLUD1 reaction that uses ammonia to make glutamate (Fig. 7a). In contrast, glutamine and glutamate labeling in liver and serum are overall decreased by CC (Extended Data Fig. 7d–7g), consistent with BAT-autonomous glutamine synthesis.

Glutamine Synthetase promotes oxygen consumption

Finally, we performed siRNA knockdown experiments in mature brown adipocytes to functionally interrogate the role of GS in norepinephrine (NE)-stimulated oxygen consumption (Fig. 7i–m). *Glul* knockdown ablates GS expression but does not affect FASN or UCP1 and only slightly decreases PPAR-γ levels (Fig. 7i). By ^{15}N-ammonia tracing, we confirmed that *Glul* knockdown reduces ^{15}N1-Gln fractional labeling compared to a scrambled *siRNA* control (Fig. 7i, 7j). Moreover, by ^{15}N2-Gln tracing, we confirmed that *Glul* knockdown also attenuates the transamination of labelled nitrogen onto glutamine to produce the ^{15}N1-Gln (Fig. 7k). Importantly, *Glul* knockdown decreases NE-stimulated oxygen consumption rate (OCR) (Fig. 7l, Extended Data Fig. 7h) while raising ammonia levels (Fig. 7m). An aberrant increase in ammonia has been shown to impair OCR in astrocytes and cancer cells [81,82]. Thus, glutamine synthetase activity may facilitate BAT thermogenesis at least in part by preventing toxic levels of ammonia from accumulating.

Discussion

In this study, we quantitate metabolite exchange activities of BAT and leg during different thermogenic conditions by combining AV metabolomics and stable isotope tracing in ad libitum fed mice. The quantitative importance of various fuels used by BAT has been unresolved partly due to the different experimental settings, techniques, and subjects often used. AV studies in the 1980s using different analytical techniques measured glucose, lactate, and amino acid usage by BAT in a cold-exposed rat model [83–87], showing some similar trends. However, notable differences were observed particularly with lactate, several amino acids (including glutamine), quantitative values, and overall metabolite coverage that likely reflects the combination of analytical, experimental, species, strain and gender differences used between studies. In our study, we used C57BL/6 male mice; it was shown that female mice have higher BAT activity, more mitochondria cristae, and more

UCP-1 induction than males [88]. Also, in humans, sex differences in thermogenic adipose tissue mass and activity have been reported [89]. Thus, it will be important to perform AV metabolomics on female mice next. Fasting and feeding conditions would also affect the major BAT fuels. Recent studies identified circulating lipoprotein-enriched lipids and acylcarnitine as BAT fuels in the fasted state, or in conditions of hyperlipidemia resulting from genetic manipulations or diets. [48,49,51,52,54,68,90–92].

The data presented here considerably expands the range of metabolite inputs and outputs for BAT (and legs within the same subjects) across multiple thermogenic conditions. Under the conditions used (ad libitum fed, 60% carbohydrate, 26% protein, 14% fat diet), these data emphasize the predominant role of glucose as a BAT fuel, and to a lesser but significant extent lactate and amino acids during cold adaptation, while additionally highlighting the importance of inter-organ communication during thermogenesis. Excitingly, this study also reveals a battery of metabolites previously unrecognized as being secreted or taken up by BAT and legs, some of which likely have important signaling functions yet to be discovered. Finally, this study also uncovered an unexpected substrate cycle by which glutamine is simultaneously catabolized and synthesized. Such a cycle could help manage nitrogen balance, but given that glutamine synthetase also hydrolyzes ATP, it may additionally reflect the growing appreciation that BAT increases UCP1-independent futile cycles during cold adaptation. In conclusion, this comprehensive and quantitative metabolic analysis reveals new information about BAT's contribution to systemic nutrient clearance, supporting its translational potential to combat obesity and cancer, and provides a necessary roadmap to guide development of effective intervention strategies.

Methods

Mice:

All research complies with all relevant ethical regulations set by the NIH, IACUC, and IBC. C57BL/6J male mice were purchased from Jackson Laboratories. Mice were housed at 22ºC with a 12h light/12h dark cycle, with free access to water and a standard chow diet (Prolab Isopro® RMH 3000). All animal experiments were approved by the University of Massachusetts Chan Medical School Institutional Animal Care and Use Committee. *Thermoneutral housing:* 8-week-old mice were placed in a thermal chamber (Model RIT330SD Power Scientific) set to 30ºC or transferred to a room controlled to 30ºC. Mice were housed at 30ºC for four weeks with free access to food and water and maintained on the standard day/night light cycle. *Cold challenge:* For the acute cold challenge, 8-week-old mice were placed at 30ºC for 4 weeks. At 12 weeks old, mice were transferred early in the morning from 30ºC to prechilled cages in a 4ºC cold room with free access to pre-chilled food and water. For the chronic cold challenge, 8-week-old mice were placed in a thermal chamber (Model RIT330SD Power Scientific) where the temperature was dropped by 4ºC per week for four weeks ending at 6ºC for the final week. All mice had free access to food and water and maintained on the standard day/night light cycle. *CL 316,243 Injection:* 8-week-old mice were transferred to a room controlled to 30ºC for 4 weeks. At 12 weeks old, mice were injected with 1mg/kg CL 316,243 in the early morning and sacked beginning

4 hours post-injection. All mice had free access to food and water and maintained on the standard day/night light cycle.

AV blood sampling and tissue processing:

At 8–9AM, ad lib fed mice were anesthetized with isoflurane using the drop method and placed on a dissection tray with a nose cone. Blood collection was completed within 5 minutes post-anesthesia. An incision below the shoulder was made and the interscapular brown adipose was lifted toward the head to expose the intact Sulzer's vein. Fine surgical scissors were used to cut the Sulzer's vein and ~40 μL of blood was collected with capillary tubes without EDTA or heparin coating. Next, the mouse was flipped and cut open to expose the diaphragm. The left ventricle was then punctured through the diaphragm and ~50–100 μL blood was collected with a 29G, ½ mL insulin syringe. Finally, the leg was dissected near the quadricep to expose the femoral vein. A 26G subQ syringe was used to puncture the femoral vein, avoiding the femoral artery. Once punctured, ~40 μL of blood was collected. For serum collection, blood samples were placed on ice in the anticoagulant-free tube for 20 min, followed by centrifugation at 10,000 x g for 10 minutes at 4ºC. The resulting supernatant was stored at −80ºC and analyzed within a week. The interscapular BAT depots and quadricep muscle tissue were either snap-frozen using a liquid nitrogen-cooled Wollenburg clamp [93] or fixed for histology. Tissues were put into 2 mL Eppendorf tubes with a pre-cooled 5 mm metal bead. The cryomill (Retsch, Newtown, PA) was pre-cooled before loading of 2 mL tubes. Once pre-cooled, the tubes were loaded, and all tissues were milled at 25 Hz for 1–2 minutes. Metal beads were removed, and tissue powder was weighed out into dry ice pre-cooled 1.5 mL Eppendorf tubes for metabolite extraction.

Tissue histology:

Tissue pieces were fixed in 10% formalin. Embedding, sectioning, and Hematoxylin and Eosin (H&E) staining was done by the UMCMS Morphological Core facility. Full slides scans were taken at 20x using a Zeiss Axio-Scan.Z1. Zeiss Zen Blue was used for image processing.

In vivo isotope tracing.

Mice from 4 weeks of temperature acclimation to 30ºC, 22ºC and 6ºC were used. Prior to isotope delivery, blood samples (~20 μL) were collected by tail bleeding for 0 min time point. [U-^{13}C,^{15}N]-Glutamine tracer was delivered retro-orbitally under anesthesia at a concentration of 0.175 g/kg of body weight using a 28G insulin syringe. [^{15}N]-NH_4Cl ammonia tracer was delivered retro-orbitally under anesthesia at a concentration of 0.04 g/kg of body weight. After 2.5-, 5-, and 15-minutes post-injection, mice were euthanized, and blood (500 μL) was collected by cardiac puncture and tissues were quickly dissected and snap frozen (< 5 s) as described above.

Soluble metabolite extraction and measurements using LC-MS:

For tissue metabolite extraction, frozen and cryomilled tissue powder (~20 mg) was mixed with 40:40:20 of acetonitrile:methanol:water to make 25 mg of tissue/mL of solvent, vortexed, and centrifuged at 16,000 x g for 10 min at 4°C. 3 μL of supernatant was injected

to LC-MS. For serum, 150 μL of extraction solvent was added to 5 μL of serum and processed the same as above tissue extraction. A quadrupole orbitrap mass spectrometer (Q Exactive; ThermoFisher Scientific) operating in negative or positive ion mode was coupled to a Vanquish UHPLC system (ThermoFisher Scientific) with electrospray ionization and used to scan from m/z 70 to 1,000 at 2 Hz, with a 140,000 resolution. LC separation was achieved on an XBridge BEH Amide column (2.1 × 150 mm^2, 2.5μm particle size, 130 Å pore size; Waters Corporation) using a gradient of solvent A (95:5 water: acetonitrile with 20 mM of ammonium acetate and 20 mM of ammonium hydroxide, pH 9.45) and solvent B (acetonitrile). Flow rate was 150μl/min. The LC gradient was: 0 min, 85% B; 2 min, 85% B; 3 min, 80% B; 5 min, 80% B; 6 min, 75% B; 7 min, 75% B; 8 min, 70% B; 9 min, 70% B; 10 min, 50% B; 12 min, 50% B; 13 min, 25% B; 16 min, 25% B; 18 min, 0% B; 23 min, 0% B; 24 min, 85% B; and 30 min, 85% B. The autosampler temperature was 5°C and the injection volume was 3μl. Metabolite concentrations were determined by authentic synthesized standards from Sigma. For pyruvate, citrate, succinate, and taurine, median values of blood concentrations in healthy male subjects from HMDB were adapted for TN and other conditions were calculated by comparing ion counts. Data were analyzed using the MAVEN software (build 682, http://maven.princeton.edu/index.php) and Compound Discoverer software (Thermofisher Scientific). Natural isotope correction for dual isotopes was performed with AccuCor2 R code (https://github.com/wangyujue23/AccuCor2) and IsoCorrectoR [94].

Circulating lipid saponification and measurements by LC-MS:

500 μL of 90% methanol, 0.3 M potassium hydroxide was added to 5 μL of serum in glass vial, vortexed and incubated in 80°C water bath for one hour, followed by immediate neutralization with 50 μL of 100% formic acid. 500 μL of hexane was added, vortexed and allowed to phase separate, before 250 μL of top layer were collected- this step was repeated, and extracts pooled. Extracts were nitrogen dried and then diluted with 100 μL of 1:1 isopropanol:methanol. 3 μL were injected for LC-MS analysis. A quadrupole orbitrap mass spectrometer (Q Exactive; ThermoFisher Scientific) operating in negative ion mode was coupled to a Vanquish UHPLC system (ThermoFisher Scientific) with electrospray ionization and used to scan from m/z 200 to 530 at 3.33 Hz, with a 140,000 resolution. LC separation was achieved on an Atlantis T3 Column (150 × 2.1mm, 3 μm particle size; Waters, Milford, MA) using a gradient of solvent A (90:10 water: methanol with 1 mM ammonium acetate and 35 mM acetic acid) and solvent B (98:2 isopropanol: methanol) with 1 mM ammonium acetate and 35 mM acetic acid). Flow rate was 150 μL/min for 0 – 16.5 minutes, 200 μL/min for 16.5 to 19 min, and 150 μL/min 19.1 to 20 min. The LC gradient was: 0 min, 25% B; 2 min, 65% B; 5.5 min, 100% B; 12.5 min, 100% B; 16.5 min, 100% B; 16.5 min, 25% B; 19 min, 25% B; 19.1 min, 25% B; and 20 min, 25% B.

Metabolite measurements using GC-MS:

Tissues (~20 mg) were extracted in 80% methanol and dried down under a nitrogen stream at 42°C. Metabolites were then derivatized at 75°C for 1 hour using MTBSTFA + 1% TBDMCS (MilliporeSigma). Samples were then injected into an 8890 GC system coupled to a 5977B single quadruple mass spectrometer (Agilent Technologies). The settings are as follows: GC inlet 250°C, transfer line 280°C, MS sources 230°C, and MS quad 150°C.

An HP-5MS capillary column (30m length, 250μm diameter, 0.25 μm film thickness) was used for separation with a flow rate of 1 mL/min and an oven gradient of 90°C for 2 mins, followed by a 10°C/min ramp to 270°C, followed by a 5°C ramp to 300°C, followed by a 6 min hold at 300°C. The MSD was run in positive ion mode using SIM measuring glutamine at 431.3, 432.3, 433.3 m/z and glutamate at 432.2, 433.2 m/z. Analysis was performed using MassHunter MS Quantitative Analysis (Agilent Technologies).

Echocardiography and Vascular Imaging:

All imaging was done in the UMass Chan Medical School Cardiovascular & Surgical Models Core (IACUC protocol #20220006). The back and chest were treated with depilatory cream. Animals were induced with 2.0% isoflurane mixed with 0.5 L/min 100% 0_2 and gently affixed in the prone position to the heated physiologic platform of the Vevo 3100 imaging system (Visualsonics, Toronto, ON, Canada). Electrode cream was applied to each limb. Body temperature was continually monitored and maintained at ~37°C with a rectal temperature probe. Isoflurane was administered by nose cone and the concentration reduced to 1.0 % isoflurane mixed with 0.5 L/min 100% 0_2. All animals were imaged at a heart rate of at least 400–500 beats per minute (bpm), any animals below 400 bpm were excluded from the analysis. A 50 MHz transducer (MX550S) was used to find the Sulzer vein. Vein flow was verified with color flow doppler. Pulsed wave doppler was used to measure flow in the Sulzer's vein. The velocity time integral (VTI) of flow was measured for three consecutive beats at end expiration. The diameter of the vein was measured with 2D doppler using the leading edge to leading edge technique and with a digital caliper, which was more reliable for CC mice and indicated that the diameter in CC is 2-times the size of TN. Flow in the Sulzer vein was calculated by multiplying the average VTI of vein flow by the cross-sectional area of the vein ($CSA = \pi r^2$) and heart rate (bpm). Flow in the Sulzer's vein was normalized to the weight of BAT tissue giving the final blood flow values of 10.93, 38.95, 17.99, 35.44 μl/s per g BAT in TN, CC, AC, and CL respectively. Mice were then placed supine for echocardiography. 2D and M-mode images were obtained in the parasternal long and parasternal short axis as previously described [95,96]. Image analysis was performed off-line using Vevo Lab image analysis software. LV volumes were derived from m-mode measurements using the following formulas: LV diastolic volume ((7.0/(2.4 + LVID;d))*LVID;d^3 and LV systolic volume ((7.0/(2.4 + LVID;s))*LVID;s^3. Cardiac output was calculated by the following equation (CO=stroke volume x heart rate). LV mass was calculated using the following formula (1.053*((LVID;d + LVPW;d + IVS;d) ^{3}-LVID;d^3).

Cell culture:

Brown preadipocytes were isolated from neonates at postnatal day 1 and immortalized with pBabe-SV40 Large T according to standard protocol [97] and as described previously [5]. The gender of each neonate was not determined. Cells were maintained in high-glucose (25 mM) DMEM in incubators at 37ºC and 5% CO_2. For brown adipocyte differentiation, cells were seeded (Day 0) at medium density and allowed to proliferate to confluence in the presence of high-glucose DMEM including 10% FBS, 1% antibiotics, 20 nM insulin and 1nM T3. After 2 days (Day 2), cells were induced by adding induction media (high-glucose DMEM including 10% FBS, 1% antibiotics, 20 nM insulin, 1 nM T3, 0.125 mM indomethacin, 2 mg/mL dexamethasone and 0.5 mM 3-isobutyl-1-methylxanthine (IBMX)) for 2 days.

After this, the medium (high-glucose DMEM including 10% FBS and 1% antibiotics) with insulin and T3 was changed every 2 days until assay. To stimulate beta-adrenergic signaling, norepinephrine (1μM) was administered directly to cells in culture.

siRNA Transfection:

siGenome siRNA pools targeting *Glul* were purchased from Horizon Discovery (Horizon# M-062120-01-0005) along with an siRNA non-target control (Horizon# D-001206-14-05). Brown adipocytes were differentiated as described above and on day 8, were reverse transfected with modifications to previously published protocols [98]. In short, 25 nM siRNA was reverse transfected using Lipofectamine RNAiMax (Thermofisher #13778150) according to the manufacturer's instructions. Cell number was determined to be 20,000 and 600,000 cells for seahorse and 12-well plates respectively. Fresh media was added two days after transfection and experiments were conducted four days after transfection.

Immunoblot analysis:

Cells were washed with PBS and lysed in protein lysis buffer (1% Triton X-100, 50 mM HEPES at pH 7.4, 150 mM NaCl, 1% glycerol, 2 mM EDTA, protease/phosphatase inhibitor cocktail). For immunoblot analysis of surgically dissected fat tissue depots, tissues were cryomilled and lysed in RIPA buffer (150 mM NaCl, 50 mM HEPES at pH 7.4, 0.1% SDS, 1% Triton X-100, 1% glycerol, 2 mM EDTA, 0.5% deoxycholate) containing a protease and phosphatase inhibitor cocktail. Protein lysates were mixed with 5X SDS sample buffer and boiled, separated by SDS-PAGE, transferred to polyvinylidene difluoride (PVDF) membrane, and subjected to immunoblot analysis. Immunoblot analysis was subsequently performed using the indicated antibodies and indicated dilutions: 1:10,000 GS (BD#610517), 1:1,000 UCP1 (CST#14670 for tissue and Abcam#ab10983 for cells), 1:5,000 VINC (SantaCruz#sc-73614), 1:5,000 GLS (ProteinTech#12855), 1:2,000 GLUD1 (ProtienTech#14299), 1:1,000 FASN (CST#3180), 1:1,000 PPARy (CST#2443).

Gene expression analysis:

RNA sequencing data are from ref. 58. Nitrogen metabolism genes were sorted by FDR significance and any genes greater than 3% FDR were excluded. From the FDR refined list, nitrogen metabolism genes were handpicked and organized in descending order of CC/TN log2 ratios. For qPCR, RNA was isolated from tissues using Qiazol (QIAGEN) and an RNeasy kit (QIAGEN). 1 μg of RNA was reverse-transcribed to cDNA using a High capacity cDNA reverse transcription kit (#4368813, Applied Biosystems). Quantitative RT-PCR (qRT-PCR) was performed in 10uL reactions using a StepOnePlus real-time PCR machine from Applied Biosystems using SYBR Green PCR master mix (CWBio#CW0955) according to manufacturer instructions. Melting curves were run on every plate for all genes to ensure the efficiency and specificity of the reaction. TATA-box binding protein (Tbp) gene expression was used for normalization. Data acquisition was performed with Applied Biosystems StepOne Software. *Glul* forward primer seqeunce (TGAACAAAGGCATCAAGCAAATG), *Glul* reverse primer sequence (CAGTCCAGGGTACGGGTCTT).

Seahorse Analysis:

Cellular mitochondrial respiration rate and extracellular acidification rate, represented as OCAR and ECAR respectively, were measured using a Seahorse XFe96 Analyzer (Agilent). Brown adipocytes were differentiated as described above and on day 8 were plated and transfected in a Seahorse 96-well plate using the siRNA transfection protocol described above. The seahorse assay was run 4-days post-transfection. For the mitochondrial stress test, cells were injected with 1 μM NE, 2.5 μM Oligomycin, 0.5 μM FCCP, and 0.5 μM Rotenone and Antimycin A. All measurements were conducted with 3 measurement cycles and 3-minute measurements except after NE injection where 10 measurement cycles were performed. Hoechst 33342 was injected during the final injection to allow normalization to cell number using the CytationV (Agilent). Maximal NE stimulated OCR was calculated by subtracting the final baseline measurement from the maximal OCR response induced from NE injection. Wave (Agilent) was used for data acquisition.

Ammonia Measurement:

Ammonia was measured by Berthelot reaction adapted from the literature [99]. In brief, media was collected from cells, and cells and tissue were lysed in 80% methanol:20% water. 20 μL of serum or 80% methanol extract was mixed with 200 μL of reagent 1 (100 mM phenol, 50 mg/L sodium nitroprusside) and 200 μL of reagent 2 (0.38M dibasic sodium phosphate, 125 mM sodium hydroxide, 1% sodium hypochlorite). Reaction mixture was placed at 37ºC for 1 hour, moved to a 96-well plate and absorbance was measured at 670nm. A standard curve was generated each time.

Statistics and Reproducibility.

Heatmaps were generated using Metaboanalyst and R 4.1.1 software (gplots). Statistical analysis was performed using Graphpad Prism 9.0 and R software (rstatix). When two groups were compared, a two-tailed, unpaired Student's t-test was used to calculate P values, with $P < 0.05$ used to determine statistical significance. When >2 groups were compared, a one-way ANOVA was employed. Tukey's method was used to correct for multiple comparisons. Bootstrapping utilizing 10,000 simulations was conducted to calculate the confidence interval of the difference between tissue and serum area under the curve. The area under the curve was calculated from values of fractional labeling versus time. Random sampling was conducted in a paired manner for tissue and serum fractional labeling from each mouse. The final confidence interval was converted into fold change by dividing the range by average serum AUC. All western blots in this study are representative of at least three independent experiments.

Extended Data

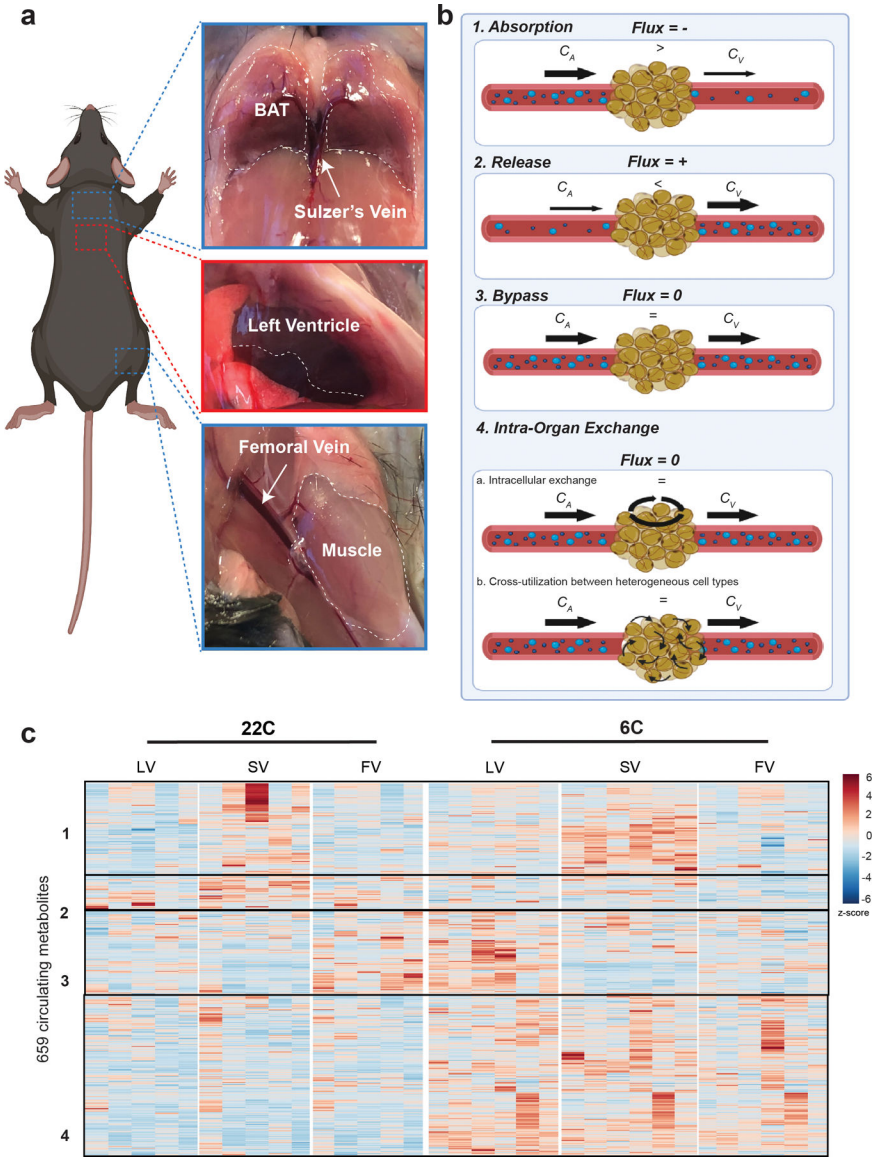

Extended Data Figure 1. Establishment of AV metabolomics for BAT and hind limb in mice.

a, Schematic of blood vessels used for AV sampling. The Sulzer's vein (SV) and femoral vein (FV) were used to characterize BAT and hind limb activity. Systemic arterial blood was collected from the left ventricle (LV). Made with BioRender.com. b, Different biological scenarios reflected by AV gradients across BAT. Positive and negative values indicate net release and absorption, while net zero values indicate metabolite bypass (neither uptake nor release). intracellular futile cycling (release equal to uptake) or intercellular cross-exchange between adipocytes and non-adipocytes. c, Heat map shows different metabolite abundances between LV, SV and FV blood collected from mice adapted to mild (22°C) or severe cold (6°C). Box 1 highlights metabolites more abundant in BAT-draining blood (SV) than blood from other sites, regardless of temperature, boxes 2–3 highlight metabolites more abundant in BAT-draining blood (SV) or systemic arterial blood (LV) and temperature-sensitive, and

box 4 highlights metabolites sensitive to temperature across organs. Each column shows an individual mouse.

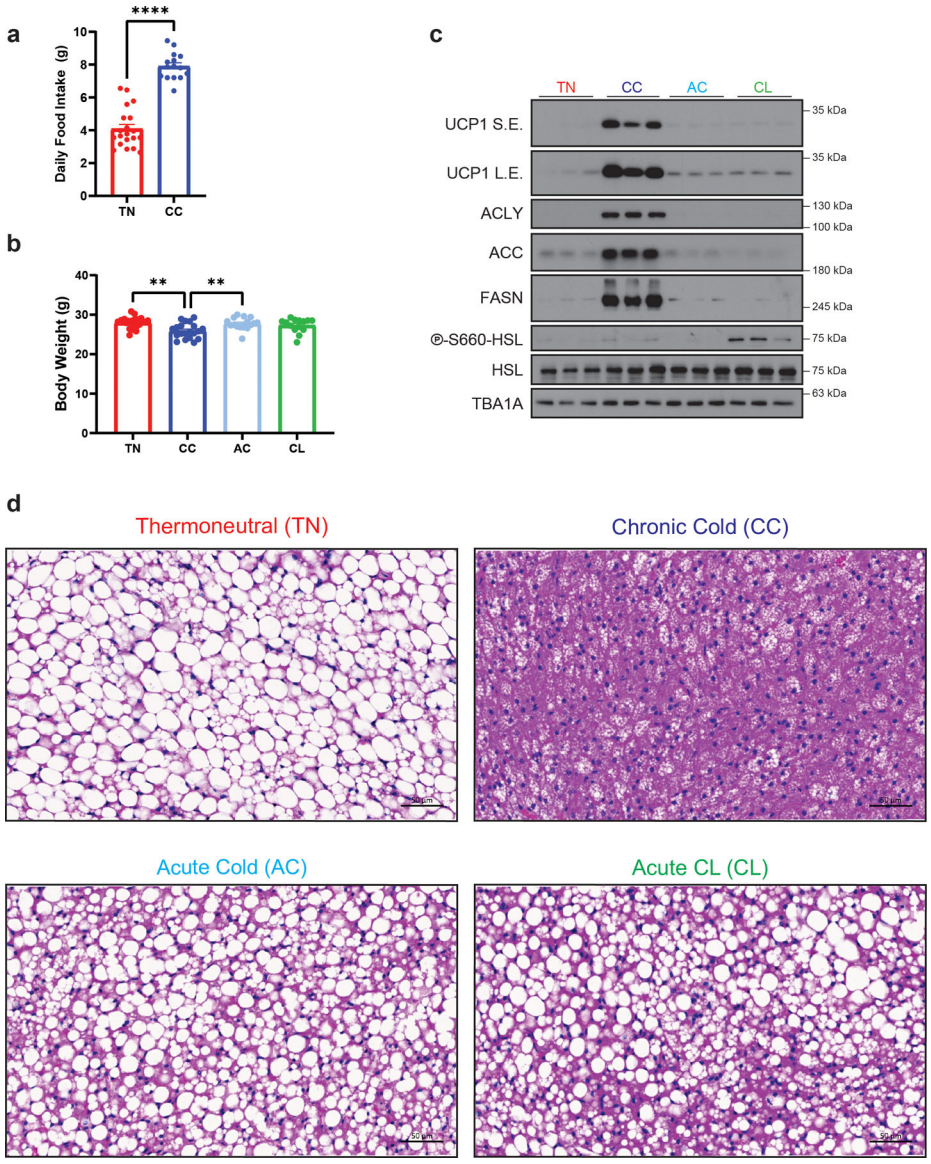

Extended Data Figure 2. Characterization of BAT in TN, CC, AC, and CL.

a, Daily food intake of TN and CC adapted mice. Data are mean ± s.e. ****$p=3\times10^{-12}$ by unpaired two-tailed Student's t-test. b, Final body weight of TN, CC, AC, CL treated mice. Data are mean ± s.e. **p=0.001 and p=0.009 by one-way ANOVA with Tukey's multiple comparisons test. c, Western blot of key markers in BAT from mice in TN, CC, AC, and CL. S.E., short exposure; L.E., long exposure. d, H&E images of BAT from mice in TN, CC, AC, and CL. Scale bar = 50 um.

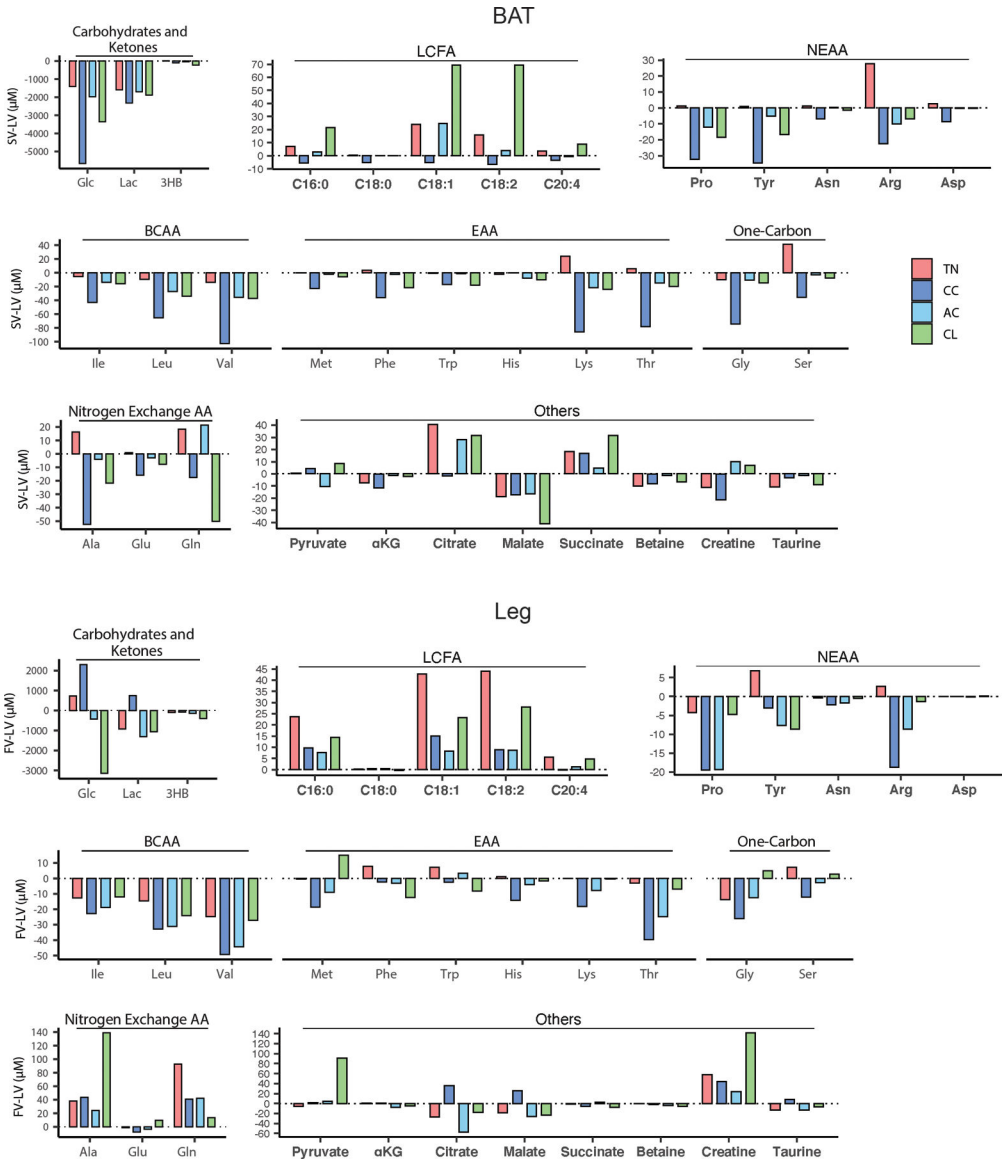

Extended Data Figure 3. AV concentration gradients of the 35 primary fuel metabolites.
Median values from mice in Figures 1–3 are shown.

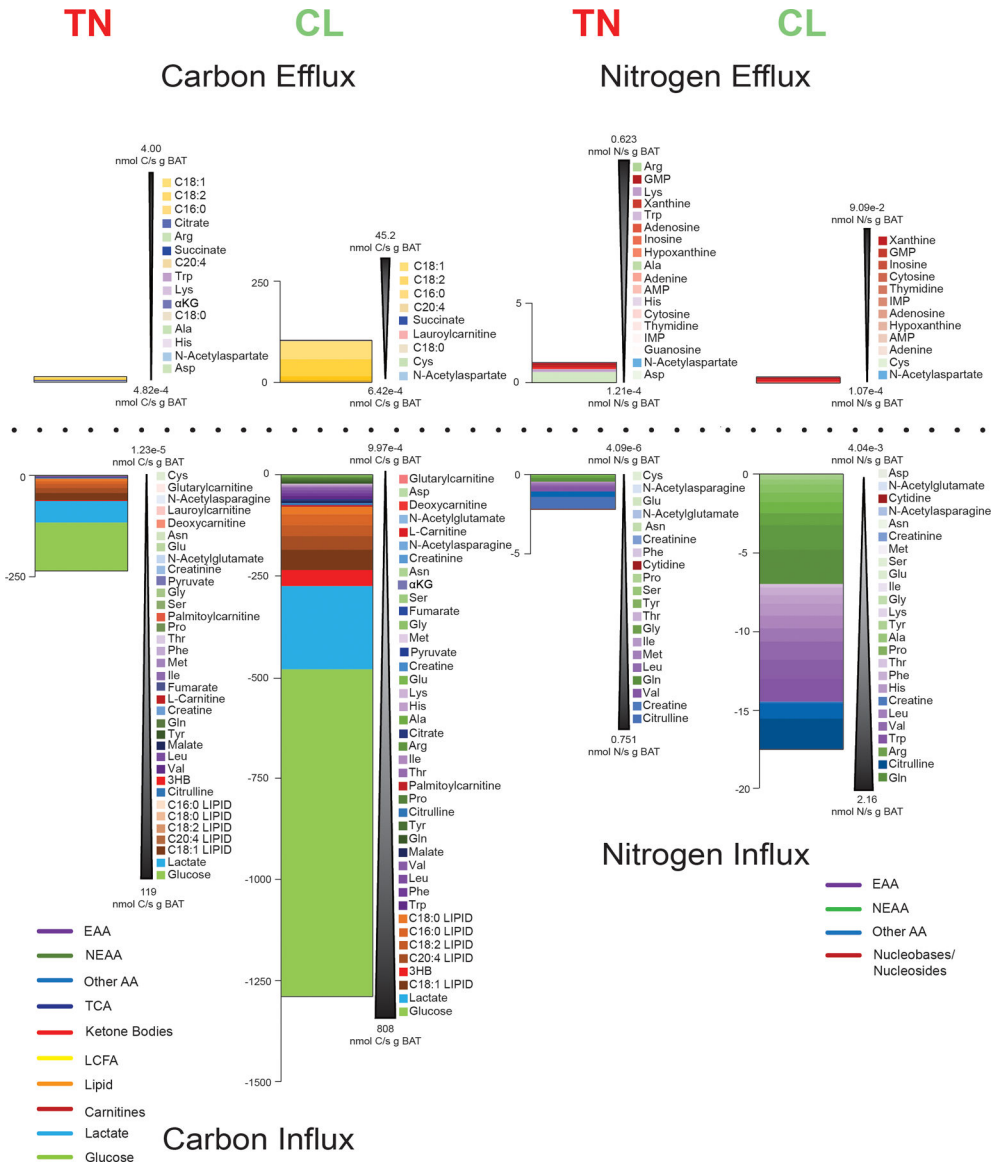

Extended Data Figure 4. Quantitative analysis of BAT total carbon and nitrogen influx and efflux in TN and CL.

Colors indicate different metabolite categories. Metabolites are ordered based on their relative contributions from greatest to least. Fatty acids from lipoprotein particles are indicated as “LIPID” after each fatty acid species (e.g., C16:0 LIPID).

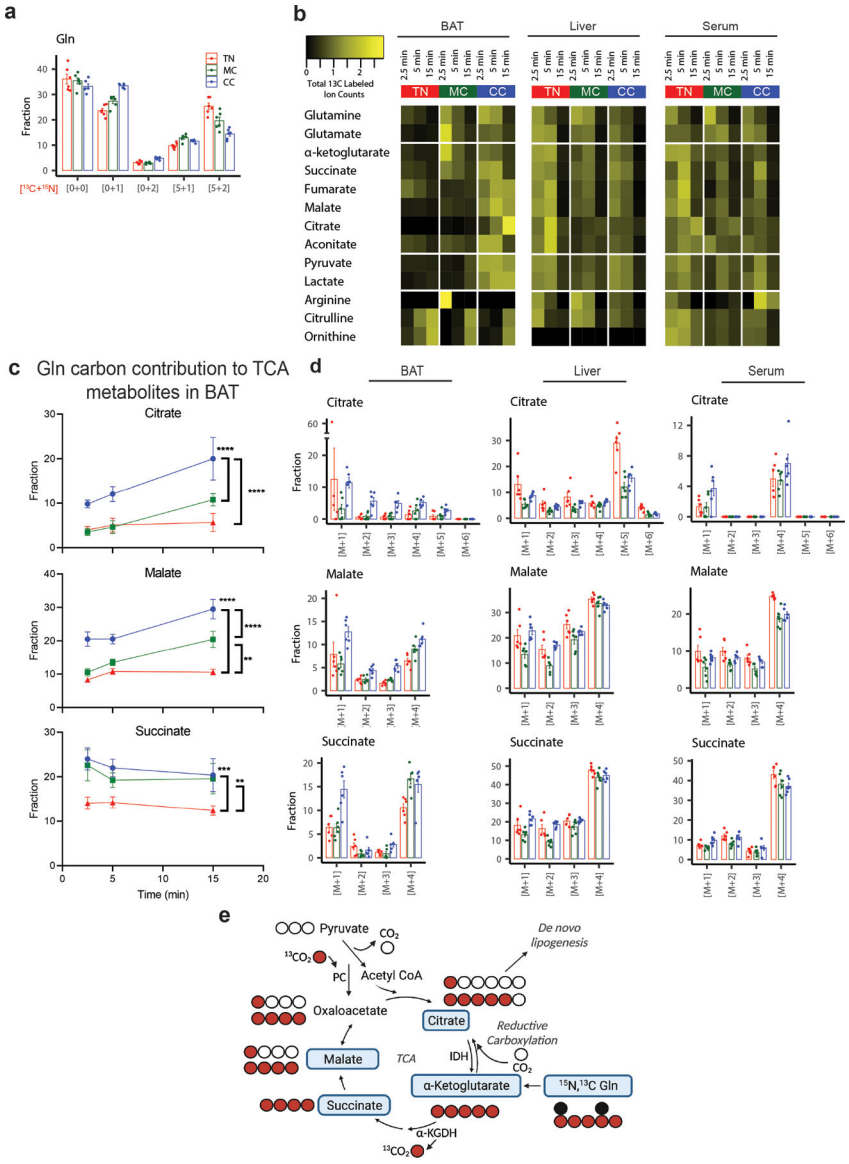

Extended Data Figure 5. Temperature-dependent glutamine carbon usage by BAT and liver.

a, Glutamine fractional labeling (both carbon and nitrogen) at 5 min after tracer administration in BAT for TN, MC and CC. Data are mean ± s.e. N=6 mice per temperature condition. b, Heatmap shows median of the total ^{13}C-labeled carbons in metabolites in BAT, liver and serum for TN, MC and CC, scaled for each metabolite and organ. N=6 mice for TN, N=6 mice for MC, N=7 mice for CC at 2.5 min, N=6 mice for all temperature conditions at 5 min, N=6 mice for TN, N=6 mice for MC, N=5 mice for CC at 15 min for BAT, and N=6 mice for all temperature conditions at 15 min for liver and serum. c, Total normalized labeling fraction of carbon atoms in representative TCA intermediates in BAT. Data are mean ± s.e. ****p<0.0001 by two-way ANOVA with post-hoc Tukey HSD Test. Malate MC vs TN **p=0.0021, Succinate CC vs TN ***p=0.0002 and MC vs TN **p=0.0027. N=6 mice for TN, N=6 mice for MC, N=7 mice for CC at 2.5 min, N=6 mice for all temperature conditions at 5 min, N=6 mice for TN, N=6 mice for MC, N=5 mice for

CC at 15 min. d, Normalized carbon labeling fraction of representative TCA intermediates at 5 min after tracer administration. Data are mean ± s.e. N=6 mice per temperature condition. e, Schematic of TCA cycle labeling from glutamine. Conventional TCA cycle predicts M+4 labeling of succinate, malate, and citrate from glutamine tracer, whereas reversed TCA cycle (i.e., reductive carboxylation) predicts M+5 labeling of citrate. PC flux can also generate M+5 citrate with labeled CO_2 incorporation. Citrate can be used for de novo lipogenesis. Made with BioRender.com.

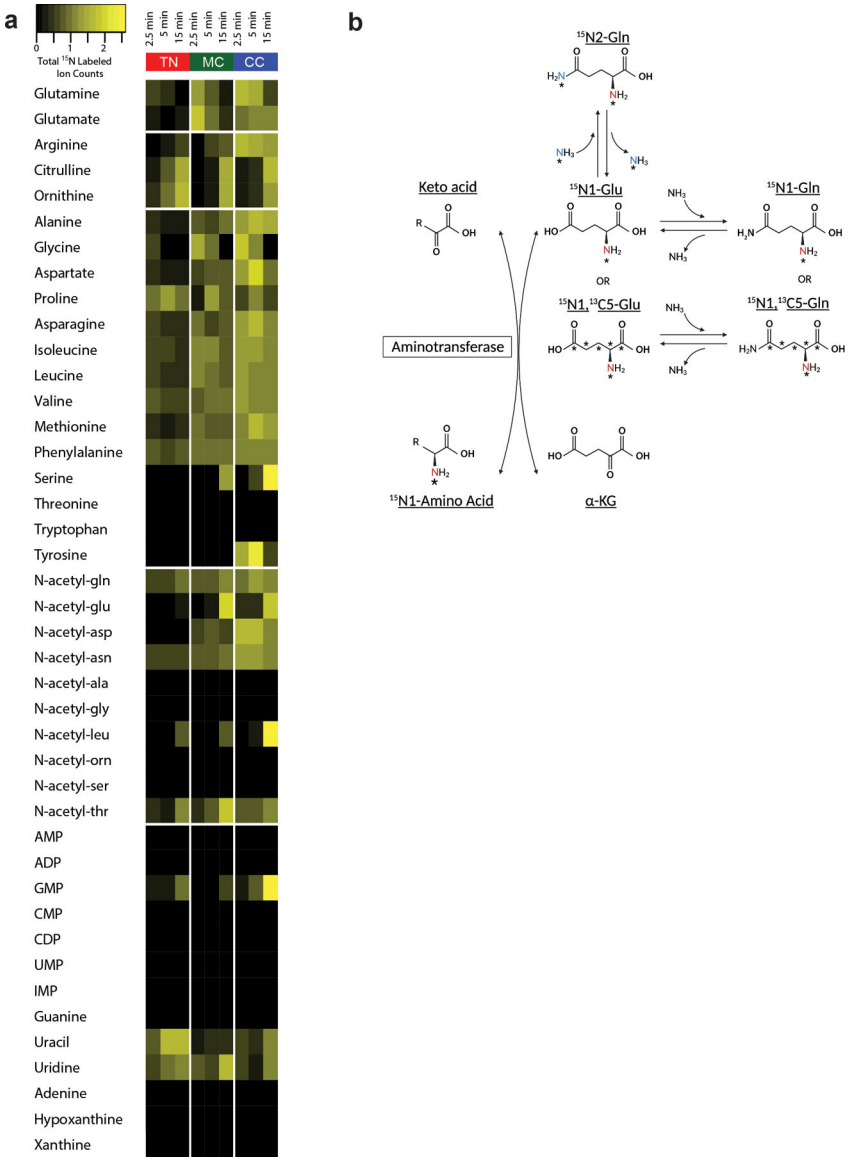

Extended Data Figure 6. Temperature-dependent glutamine nitrogen usage by BAT.
a, Heatmap shows median of total ^{15}N-labeled nitrogen in BAT metabolites for TN, MC and CC. N=6 mice for TN, N=6 mice for MC, N=7 mice for CC at 2.5 min, N=6 mice for all temperature conditions at 5 min, N=6 mice for TN, N=6 mice for MC, N=5 mice for CC at 15 min. b, Schematic of nitrogen exchange reactions between glutamine, glutamate and keto acids. Made with BioRender.com.

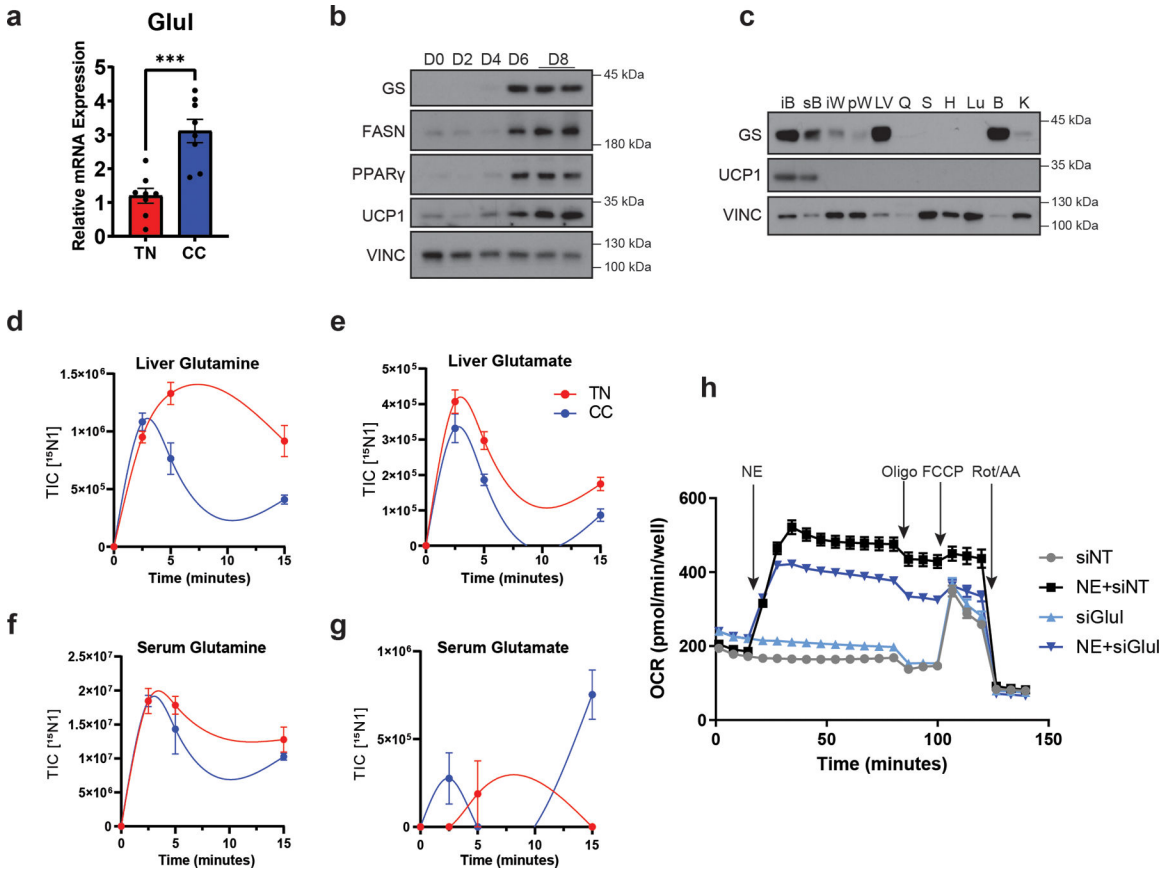

Extended Data Figure 7. Cold-induced glutamine synthetase in BAT.

a, qRT-PCR comparing Glul gene expression in BAT for TN and CC. N=8 mice per condition. Data are mean ± s.e. ***p=0.0003 by unpaired two-tailed Student's t-test. b, Western blot of GS in brown adipocytes during adipogenesis. c, Western blot of GS in different tissues from mice at 22°C. iB, interscapular BAT; sB, subcutaneous BAT; iW, inguinal white fat; pW, perigonadal white fat; LV, liver; Q, quadricep; S, spleen; H, heart; Lu, lung; B, brain; K, kidney. d-g, ^{15}N1-labeled glutamine and glutamate abundances in liver (d,e) or serum (f,g) after ^{15}N-ammonia tracer administration. N=5 mice were used for each time point except TN 15-minute and CC 5-minute N=4 mice were used. Data are mean ± s.e. h, Full graph of oxygen consumption rate in mature brown adipocytes transfected with control or Glul targeting siRNAs with or without norepinephrine (NE) stimulation. N=15 biological replicates. Data are mean ± s.e.

Supplementary Material

Refer to Web version on PubMed Central for supplementary material.

Acknowledgments

We thank all members of the Jang and Guertin laboratories for the discussion. We thank Jinsu Park for help with bootstrapping and statistical methods, and Fred Roberts and Timothy Cashman for their technical assistance with blood flow measurements.

Funding:

This work was funded by R01DK116005, R01DK127175 and R01DK094004 to D.A.G.; the AASLD Foundation Pinnacle Research Award in Liver Disease, the Edward Mallinckrodt, Jr. Foundation Award, and NIH/NIAAA R01 AA029124 to C.J; F31DK129018 to J.A.H; T32GM008620 and F31DK134173 to J.L; Basic Science Research Program of the Ministry of Education (MOE, South Korea) NRF-2019R1A6A1A10073079 to S.M.J. R01HL118100 and R01HL141377 to C.M.T.

References

1. Cannon B & Nedergaard J Brown adipose tissue: function and physiological significance. Physiol Rev 84, 277–359, doi:10.1152/physrev.00015.2003 (2004). [PubMed: 14715917]
2. Rothwell NJ & Stock MJ A role for brown adipose tissue in diet-induced thermogenesis. Nature 281, 31–35, doi:10.1038/281031a0 (1979). [PubMed: 551265]
3. Feldmann HM, Golozoubova V, Cannon B & Nedergaard J UCP1 ablation induces obesity and abolishes diet-induced thermogenesis in mice exempt from thermal stress by living at thermoneutrality. Cell metabolism 9, 203–209, doi:10.1016/j.cmet.2008.12.014 (2009). [PubMed: 19187776]
4. von Essen G, Lindsund E, Cannon B & Nedergaard J Adaptive facultative diet-induced thermogenesis in wild-type but not in UCP1-ablated mice. Am J Physiol Endocrinol Metab 313, E515–E527, doi:10.1152/ajpendo.00097.2017 (2017). [PubMed: 28679625]
5. Hung CM et al. Rictor/mTORC2 loss in the Myf5 lineage reprograms brown fat metabolism and protects mice against obesity and metabolic disease. Cell Rep 8, 256–271, doi:10.1016/j.celrep.2014.06.007 (2014). [PubMed: 25001283]
6. Jung SM et al. Non-canonical mTORC2 Signaling Regulates Brown Adipocyte Lipid Catabolism through SIRT6-FoxO1. Mol Cell 75, 807–822 e808, doi:10.1016/j.molcel.2019.07.023 (2019). [PubMed: 31442424]
7. Nedergaard J & Cannon B Diet-Induced Thermogenesis: Principles and Pitfalls. Methods Mol Biol 2448, 177–202, doi:10.1007/978-1-0716-2087-8_12 (2022). [PubMed: 35167098]
8. Betz MJ & Enerback S Targeting thermogenesis in brown fat and muscle to treat obesity and metabolic disease. Nat Rev Endocrinol 14, 77–87, doi:10.1038/nrendo.2017.132 (2018). [PubMed: 29052591]
9. Cypess AM et al. Identification and importance of brown adipose tissue in adult humans. N Engl J Med 360, 1509–1517, doi:10.1056/NEJMoa0810780 (2009). [PubMed: 19357406]
10. Nedergaard J, Bengtsson T & Cannon B Unexpected evidence for active brown adipose tissue in adult humans. Am J Physiol Endocrinol Metab 293, E444–452, doi:10.1152/ajpendo.00691.2006 (2007). [PubMed: 17473055]
11. Saito M et al. High incidence of metabolically active brown adipose tissue in healthy adult humans: effects of cold exposure and adiposity. Diabetes 58, 1526–1531, doi:10.2337/db09-0530 (2009). [PubMed: 19401428]
12. van Marken Lichtenbelt WD et al. Cold-activated brown adipose tissue in healthy men. N Engl J Med 360, 1500–1508, doi:10.1056/NEJMoa0808718 (2009). [PubMed: 19357405]
13. Virtanen KA et al. Functional brown adipose tissue in healthy adults. N Engl J Med 360, 1518–1525, doi:10.1056/NEJMoa0808949 (2009). [PubMed: 19357407]
14. Chen KY et al. Opportunities and challenges in the therapeutic activation of human energy expenditure and thermogenesis to manage obesity. J Biol Chem 295, 1926–1942, doi:10.1074/jbc.REV119.007363 (2020). [PubMed: 31914415]
15. Wolfrum C & Gerhart-Hines Z Fueling the fire of adipose thermogenesis. Science 375, 1229–1231, doi:10.1126/science.abl7108 (2022). [PubMed: 35298244]
16. Seki T et al. Brown-fat-mediated tumour suppression by cold-altered global metabolism. Nature 608, 421–428, doi:10.1038/s41586-022-05030-3 (2022). [PubMed: 35922508]
17. Hui S et al. Quantitative Fluxomics of Circulating Metabolites. Cell metabolism 32, 676–688 e674, doi:10.1016/j.cmet.2020.07.013 (2020). [PubMed: 32791100]
18. Villarroya F, Cereijo R, Villarroya J & Giralt M Brown adipose tissue as a secretory organ. Nat Rev Endocrinol 13, 26–35, doi:10.1038/nrendo.2016.136 (2017). [PubMed: 27616452]

19. Cereijo R et al. CXCL14, a Brown Adipokine that Mediates Brown-Fat-to-Macrophage Communication in Thermogenic Adaptation. Cell metabolism 28, 750–763 e756, doi:10.1016/j.cmet.2018.07.015 (2018). [PubMed: 30122557]
20. Wang Z et al. Chronic cold exposure enhances glucose oxidation in brown adipose tissue. EMBO Rep 21, e50085, doi:10.15252/embr.202050085 (2020). [PubMed: 33043581]
21. Trayhurn P Fatty acid synthesis in vivo in brown adipose tissue, liver and white adipose tissue of the cold-acclimated rat. FEBS Lett 104, 13–16, doi:10.1016/0014-5793(79)81075-3 (1979). [PubMed: 477972]
22. Foster DO, Frydman ML & Usher JR Nonshivering thermogenesis in the rat. I. The relation between drug-induced changes in thermogenesis and changes in the concentration of plasma cyclic AMP. Can J Physiol Pharmacol 55, 52–64, doi:10.1139/y77-008 (1977). [PubMed: 191171]
23. Foster DO & Frydman ML Nonshivering thermogenesis in the rat. II. Measurements of blood flow with microspheres point to brown adipose tissue as the dominant site of the calorigenesis induced by noradrenaline. Can J Physiol Pharmacol 56, 110–122, doi:10.1139/y78-015 (1978). [PubMed: 638848]
24. Foster DO & Frydman ML Tissue distribution of cold-induced thermogenesis in conscious warm- or cold-acclimated rats reevaluated from changes in tissue blood flow: the dominant role of brown adipose tissue in the replacement of shivering by nonshivering thermogenesis. Can J Physiol Pharmacol 57, 257–270, doi:10.1139/y79-039 (1979). [PubMed: 445227]
25. Lopez-Soriano FJ & Alemany M Effect of cold-temperature exposure and acclimation on amino acid pool changes and enzyme activities of rat brown adipose tissue. Biochim Biophys Acta 925, 265–271, doi:10.1016/0304-4165(87)90191-7 (1987). [PubMed: 2887209]
26. Jang C, Chen L & Rabinowitz JD Metabolomics and Isotope Tracing. Cell 173, 822–837, doi:10.1016/j.cell.2018.03.055 (2018). [PubMed: 29727671]
27. Murashige D et al. Comprehensive quantification of fuel use by the failing and nonfailing human heart. Science 370, 364–368, doi:10.1126/science.abc8861 (2020). [PubMed: 33060364]
28. Jang C et al. Metabolite Exchange between Mammalian Organs Quantified in Pigs. Cell metabolism 30, 594–606 e593, doi:10.1016/j.cmet.2019.06.002 (2019). [PubMed: 31257152]
29. Berg F, Gustafson U & Andersson L The uncoupling protein 1 gene (UCP1) is disrupted in the pig lineage: a genetic explanation for poor thermoregulation in piglets. PLoS Genet 2, e129, doi:10.1371/journal.pgen.0020129 (2006). [PubMed: 16933999]
30. Hou L et al. Pig has no uncoupling protein 1. Biochem Biophys Res Commun 487, 795–800, doi:10.1016/j.bbrc.2017.04.118 (2017). [PubMed: 28442343]
31. Dou H et al. Aryl hydrocarbon receptor (AhR) regulates adipocyte differentiation by assembling CRL4B ubiquitin ligase to target PPARgamma for proteasomal degradation. J Biol Chem 294, 18504–18515, doi:10.1074/jbc.RA119.009282 (2019). [PubMed: 31653699]
32. Gnad T et al. Adenosine activates brown adipose tissue and recruits beige adipocytes via A2A receptors. Nature 516, 395–399, doi:10.1038/nature13816 (2014). [PubMed: 25317558]
33. Lahesmaa M et al. Regulation of human brown adipose tissue by adenosine and A2A receptors - studies with [(15)O]H2O and [(11)C]TMSX PET/CT. Eur J Nucl Med Mol Imaging 46, 743–750, doi:10.1007/s00259-018-4120-2 (2019). [PubMed: 30105585]
34. Hui S et al. Glucose feeds the TCA cycle via circulating lactate. Nature 551, 115–118, doi:10.1038/nature24057 (2017). [PubMed: 29045397]
35. Yoneshiro T et al. Metabolic flexibility via mitochondrial BCAA carrier SLC25A44 is required for optimal fever. Elife 10, doi:10.7554/eLife.66865 (2021).
36. Yoneshiro T et al. BCAA catabolism in brown fat controls energy homeostasis through SLC25A44. Nature 572, 614–619, doi:10.1038/s41586-019-1503-x (2019). [PubMed: 31435015]
37. Keinan O et al. Glycogen metabolism links glucose homeostasis to thermogenesis in adipocytes. Nature 599, 296–301, doi:10.1038/s41586-021-04019-8 (2021). [PubMed: 34707293]
38. Jung SM et al. In vivo isotope tracing reveals the versatility of glucose as a brown adipose tissue substrate. Cell Rep 36, 109459, doi:10.1016/j.celrep.2021.109459 (2021). [PubMed: 34320357]
39. Jabbour HN & Sales KJ Prostaglandin receptor signalling and function in human endometrial pathology. Trends Endocrinol Metab 15, 398–404, doi:10.1016/j.tem.2004.08.006 (2004). [PubMed: 15380812]

40. Cekic C & Linden J Purinergic regulation of the immune system. Nat Rev Immunol 16, 177–192, doi:10.1038/nri.2016.4 (2016). [PubMed: 26922909]
41. Di Virgilio F, Sarti AC, Falzoni S, De Marchi E & Adinolfi E Extracellular ATP and P2 purinergic signalling in the tumour microenvironment. Nat Rev Cancer 18, 601–618, doi:10.1038/s41568-018-0037-0 (2018). [PubMed: 30006588]
42. Boldyrev AA, Aldini G & Derave W Physiology and pathophysiology of carnosine. Physiol Rev 93, 1803–1845, doi:10.1152/physrev.00039.2012 (2013). [PubMed: 24137022]
43. Schaalan MF, Ramadan BK & Abd Elwahab AH Synergistic effect of carnosine on browning of adipose tissue in exercised obese rats; a focus on circulating irisin levels. J Cell Physiol 233, 5044–5057, doi:10.1002/jcp.26370 (2018). [PubMed: 29236301]
44. Anderson EJ et al. A carnosine analog mitigates metabolic disorders of obesity by reducing carbonyl stress. J Clin Invest 128, 5280–5293, doi:10.1172/JCI94307 (2018). [PubMed: 30226473]
45. Wolfe RR Branched-chain amino acids and muscle protein synthesis in humans: myth or reality? J Int Soc Sports Nutr 14, 30, doi:10.1186/s12970-017-0184-9 (2017). [PubMed: 28852372]
46. Laha A, Singh M, George AK, Homme RP & Tyagi SC Dysregulation of 1-carbon metabolism and muscle atrophy: potential roles of forkhead box O proteins and PPARgamma co-activator-1alpha. Can J Physiol Pharmacol 97, 1013–1017, doi:10.1139/cjpp-2019-0227 (2019). [PubMed: 31269408]
47. Ye J et al. Serine catabolism regulates mitochondrial redox control during hypoxia. Cancer Discov 4, 1406–1417, doi:10.1158/2159-8290.CD-14-0250 (2014). [PubMed: 25186948]
48. Bartelt A et al. Brown adipose tissue activity controls triglyceride clearance. Nat Med 17, 200–205, doi:10.1038/nm.2297 (2011). [PubMed: 21258337]
49. Heine M et al. Lipolysis Triggers a Systemic Insulin Response Essential for Efficient Energy Replenishment of Activated Brown Adipose Tissue in Mice. Cell metabolism 28, 644–655 e644, doi:10.1016/j.cmet.2018.06.020 (2018). [PubMed: 30033199]
50. Fischer AW et al. Lysosomal lipoprotein processing in endothelial cells stimulates adipose tissue thermogenic adaptation. Cell metabolism 33, 547–564 e547, doi:10.1016/j.cmet.2020.12.001 (2021). [PubMed: 33357458]
51. Fischer AW et al. Brown adipose tissue lipoprotein and glucose disposal is not determined by thermogenesis in uncoupling protein 1-deficient mice. J Lipid Res 61, 1377–1389, doi:10.1194/jlr.RA119000455 (2020). [PubMed: 32769145]
52. Berbee JF et al. Brown fat activation reduces hypercholesterolaemia and protects from atherosclerosis development. Nat Commun 6, 6356, doi:10.1038/ncomms7356 (2015). [PubMed: 25754609]
53. Wade G, McGahee A, Ntambi JM & Simcox J Lipid Transport in Brown Adipocyte Thermogenesis. Front Physiol 12, 787535, doi:10.3389/fphys.2021.787535 (2021). [PubMed: 35002769]
54. Simcox J et al. Global Analysis of Plasma Lipids Identifies Liver-Derived Acylcarnitines as a Fuel Source for Brown Fat Thermogenesis. Cell metabolism 26, 509–522 e506, doi:10.1016/j.cmet.2017.08.006 (2017). [PubMed: 28877455]
55. M, U. D. et al. Postprandial Oxidative Metabolism of Human Brown Fat Indicates Thermogenesis. Cell metabolism 28, 207–216 e203, doi:10.1016/j.cmet.2018.05.020 (2018). [PubMed: 29909972]
56. Adlanmerini M et al. Circadian lipid synthesis in brown fat maintains murine body temperature during chronic cold. Proc Natl Acad Sci U S A 116, 18691–18699, doi:10.1073/pnas.1909883116 (2019). [PubMed: 31451658]
57. Fedorenko A, Lishko PV & Kirichok Y Mechanism of fatty-acid-dependent UCP1 uncoupling in brown fat mitochondria. Cell 151, 400–413, doi:10.1016/j.cell.2012.09.010 (2012). [PubMed: 23063128]
58. Mottillo EP et al. Coupling of lipolysis and de novo lipogenesis in brown, beige, and white adipose tissues during chronic beta3-adrenergic receptor activation. J Lipid Res 55, 2276–2286, doi:10.1194/jlr.M050005 (2014). [PubMed: 25193997]

59. Sanchez-Gurmaches J et al. Brown Fat AKT2 Is a Cold-Induced Kinase that Stimulates ChREBP-Mediated De Novo Lipogenesis to Optimize Fuel Storage and Thermogenesis. Cell metabolism 27, 195–209 e196, doi:10.1016/j.cmet.2017.10.008 (2018). [PubMed: 29153407]
60. Veliova M et al. Blocking mitochondrial pyruvate import in brown adipocytes induces energy wasting via lipid cycling. EMBO Rep 21, e49634, doi:10.15252/embr.201949634 (2020). [PubMed: 33275313]
61. Mills EL et al. Accumulation of succinate controls activation of adipose tissue thermogenesis. Nature 560, 102–106, doi:10.1038/s41586-018-0353-2 (2018). [PubMed: 30022159]
62. Bisbach CM et al. Succinate Can Shuttle Reducing Power from the Hypoxic Retina to the O(2)-Rich Pigment Epithelium. Cell Rep 31, 107606, doi:10.1016/j.celrep.2020.107606 (2020). [PubMed: 32375026]
63. Heim T & Hull D The blood flow and oxygen consumption of brown adipose tissue in the new-born rabbit. J Physiol 186, 42–55, doi:10.1113/jphysiol.1966.sp008019 (1966). [PubMed: 5914257]
64. Foster DO & Frydman ML Brown adipose tissue: the dominant site of nonshivering thermogenesis in the rat. Experientia Suppl 32, 147–151, doi:10.1007/978-3-0348-5559-4_16 (1978). [PubMed: 274305]
65. Foster DO, Depocas F & Frydman ML Noradrenaline-induced calorigenesis in warm- and cold-acclimated rats: relations between concentration of noradrenaline in arterial plasma, blood flow to differently located masses of brown adipose tissue, and calorigenic response. Can J Physiol Pharmacol 58, 915–924, doi:10.1139/y80-140 (1980). [PubMed: 7225930]
66. Bean C et al. The mitochondrial protein Opa1 promotes adipocyte browning that is dependent on urea cycle metabolites. Nat Metab 3, 1633–1647, doi:10.1038/s42255-021-00497-2 (2021). [PubMed: 34873337]
67. Ramirez AK et al. Integrating Extracellular Flux Measurements and Genome-Scale Modeling Reveals Differences between Brown and White Adipocytes. Cell Rep 21, 3040–3048, doi:10.1016/j.celrep.2017.11.065 (2017). [PubMed: 29241534]
68. Wang CH et al. CRISPR-engineered human brown-like adipocytes prevent diet-induced obesity and ameliorate metabolic syndrome in mice. Sci Transl Med 12, doi:10.1126/scitranslmed.aaz8664 (2020).
69. Labbe SM et al. mTORC1 is Required for Brown Adipose Tissue Recruitment and Metabolic Adaptation to Cold. Sci Rep 6, 37223, doi:10.1038/srep37223 (2016). [PubMed: 27876792]
70. Villarroya J et al. New insights into the secretory functions of brown adipose tissue. J Endocrinol 243, R19–R27, doi:10.1530/JOE-19-0295 (2019). [PubMed: 31419785]
71. Scheele C & Wolfrum C Brown Adipose Crosstalk in Tissue Plasticity and Human Metabolism. Endocr Rev 41, doi:10.1210/endrev/bnz007 (2020).
72. Niemann B et al. Apoptotic brown adipocytes enhance energy expenditure via extracellular inosine. Nature, doi:10.1038/s41586-022-05041-0 (2022).
73. Gnad T et al. Adenosine/A2B Receptor Signaling Ameliorates the Effects of Aging and Counteracts Obesity. Cell metabolism 34, 649, doi:10.1016/j.cmet.2022.02.014 (2022). [PubMed: 35385706]
74. Yoo H, Antoniewicz MR, Stephanopoulos G & Kelleher JK Quantifying reductive carboxylation flux of glutamine to lipid in a brown adipocyte cell line. J Biol Chem 283, 20621–20627, doi:10.1074/jbc.M706494200 (2008). [PubMed: 18364355]
75. Mullen AR et al. Reductive carboxylation supports growth in tumour cells with defective mitochondria. Nature 481, 385–388, doi:10.1038/nature10642 (2011). [PubMed: 22101431]
76. Metallo CM et al. Reductive glutamine metabolism by IDH1 mediates lipogenesis under hypoxia. Nature 481, 380–384, doi:10.1038/nature10602 (2011). [PubMed: 22101433]
77. McCormack JG & Denton RM Evidence that fatty acid synthesis in the interscapular brown adipose tissue of cold-adapted rats is increased in vivo by insulin by mechanisms involving parallel activation of pyruvate dehydrogenase and acetyl-coenzyme A carboxylase. Biochem J 166, 627–630, doi:10.1042/bj1660627 (1977). [PubMed: 23106]

78. Shimazu T & Takahashi A Stimulation of hypothalamic nuclei has differential effects on lipid synthesis in brown and white adipose tissue. Nature 284, 62–63, doi:10.1038/284062a0 (1980). [PubMed: 6444457]

79. Yu XX, Lewin DA, Forrest W & Adams SH Cold elicits the simultaneous induction of fatty acid synthesis and beta-oxidation in murine brown adipose tissue: prediction from differential gene expression and confirmation in vivo. FASEB J 16, 155–168, doi:10.1096/fj.01-0568com (2002). [PubMed: 11818363]

80. Weir G et al. Substantial Metabolic Activity of Human Brown Adipose Tissue during Warm Conditions and Cold-Induced Lipolysis of Local Triglycerides. Cell metabolism 27, 1348–1355 e1344, doi:10.1016/j.cmet.2018.04.020 (2018). [PubMed: 29805098]

81. Imai K, Tsujisaki M & Yachi A [Application of monoclonal antibodies to cancer therapy: idiotype mapping of monoclonal antibodies to tumor-associated antigens]. Gan To Kagaku Ryoho 15, 1051–1059 (1988). [PubMed: 3291766]

82. Spinelli JB et al. Metabolic recycling of ammonia via glutamate dehydrogenase supports breast cancer biomass. Science 358, 941–946, doi:10.1126/science.aam9305 (2017). [PubMed: 29025995]

83. Isler D, Hill HP & Meier MK Glucose metabolism in isolated brown adipocytes under beta-adrenergic stimulation. Quantitative contribution of glucose to total thermogenesis. Biochem J 245, 789–793, doi:10.1042/bj2450789 (1987). [PubMed: 3311035]

84. Ma SW & Foster DO Uptake of glucose and release of fatty acids and glycerol by rat brown adipose tissue in vivo. Can J Physiol Pharmacol 64, 609–614, doi:10.1139/y86-101 (1986). [PubMed: 3730946]

85. Saggerson ED, McAllister TW & Baht HS Lipogenesis in rat brown adipocytes. Effects of insulin and noradrenaline, contributions from glucose and lactate as precursors and comparisons with white adipocytes. Biochem J 251, 701–709, doi:10.1042/bj2510701 (1988). [PubMed: 3137922]

86. Lopez-Soriano FJ & Alemany M Activities of enzymes of amino acid metabolism in rat brown adipose tissue. Biochem Int 12, 471–478 (1986). [PubMed: 2871838]

87. Lopez-Soriano FJ et al. Amino acid and glucose uptake by rat brown adipose tissue. Effect of cold-exposure and acclimation. Biochem J 252, 843–849, doi:10.1042/bj2520843 (1988). [PubMed: 3421924]

88. Kaikaew K, Grefhorst A & Visser JA Sex Differences in Brown Adipose Tissue Function: Sex Hormones, Glucocorticoids, and Their Crosstalk. Front Endocrinol (Lausanne) 12, 652444, doi:10.3389/fendo.2021.652444 (2021). [PubMed: 33927694]

89. Keuper M & Jastroch M The good and the BAT of metabolic sex differences in thermogenic human adipose tissue. Mol Cell Endocrinol 533, 111337, doi:10.1016/j.mce.2021.111337 (2021). [PubMed: 34062167]

90. Ouellet V et al. Brown adipose tissue oxidative metabolism contributes to energy expenditure during acute cold exposure in humans. J Clin Invest 122, 545–552, doi:10.1172/JCI60433 (2012). [PubMed: 22269323]

91. Carneheim C, Nedergaard J & Cannon B Beta-adrenergic stimulation of lipoprotein lipase in rat brown adipose tissue during acclimation to cold. Am J Physiol 246, E327–333, doi:10.1152/ajpendo.1984.246.4.E327 (1984). [PubMed: 6372506]

92. Schreiber R et al. Cold-Induced Thermogenesis Depends on ATGL-Mediated Lipolysis in Cardiac Muscle, but Not Brown Adipose Tissue. Cell metabolism 26, 753–763 e757, doi:10.1016/j.cmet.2017.09.004 (2017). [PubMed: 28988821]

93. Wollenberger A, Ristau O & Schoffa G [A simple technic for extremely rapid freezing of large pieces of tissue]. Pflugers Arch Gesamte Physiol Menschen Tiere 270, 399–412 (1960).

94. Heinrich P et al. Correcting for natural isotope abundance and tracer impurity in MS-, MS/MS- and high-resolution-multiple-tracer-data from stable isotope labeling experiments with IsoCorrectoR. Sci Rep 8, 17910, doi:10.1038/s41598-018-36293-4 (2018). [PubMed: 30559398]

95. Respress JL & Wehrens XH Transthoracic echocardiography in mice. J Vis Exp, doi:10.3791/1738 (2010).

96. Scherrer-Crosbie M & Thibault HB Echocardiography in translational research: of mice and men. J Am Soc Echocardiogr 21, 1083–1092, doi:10.1016/j.echo.2008.07.001 (2008). [PubMed: 18723318]

97. Fasshauer M et al. Essential role of insulin receptor substrate 1 in differentiation of brown adipocytes. Mol Cell Biol 21, 319–329, doi:10.1128/MCB.21.1.319-329.2001 (2001). [PubMed: 11113206]

98. Isidor MS et al. An siRNA-based method for efficient silencing of gene expression in mature brown adipocytes. Adipocyte 5, 175–185, doi:10.1080/21623945.2015.1111972 (2016). [PubMed: 27386153]

99. Spinelli JB, Kelley LP & Haigis MC An LC-MS Approach to Quantitative Measurement of Ammonia Isotopologues. Sci Rep 7, 10304, doi:10.1038/s41598-017-09993-6 (2017). [PubMed: 28871132]

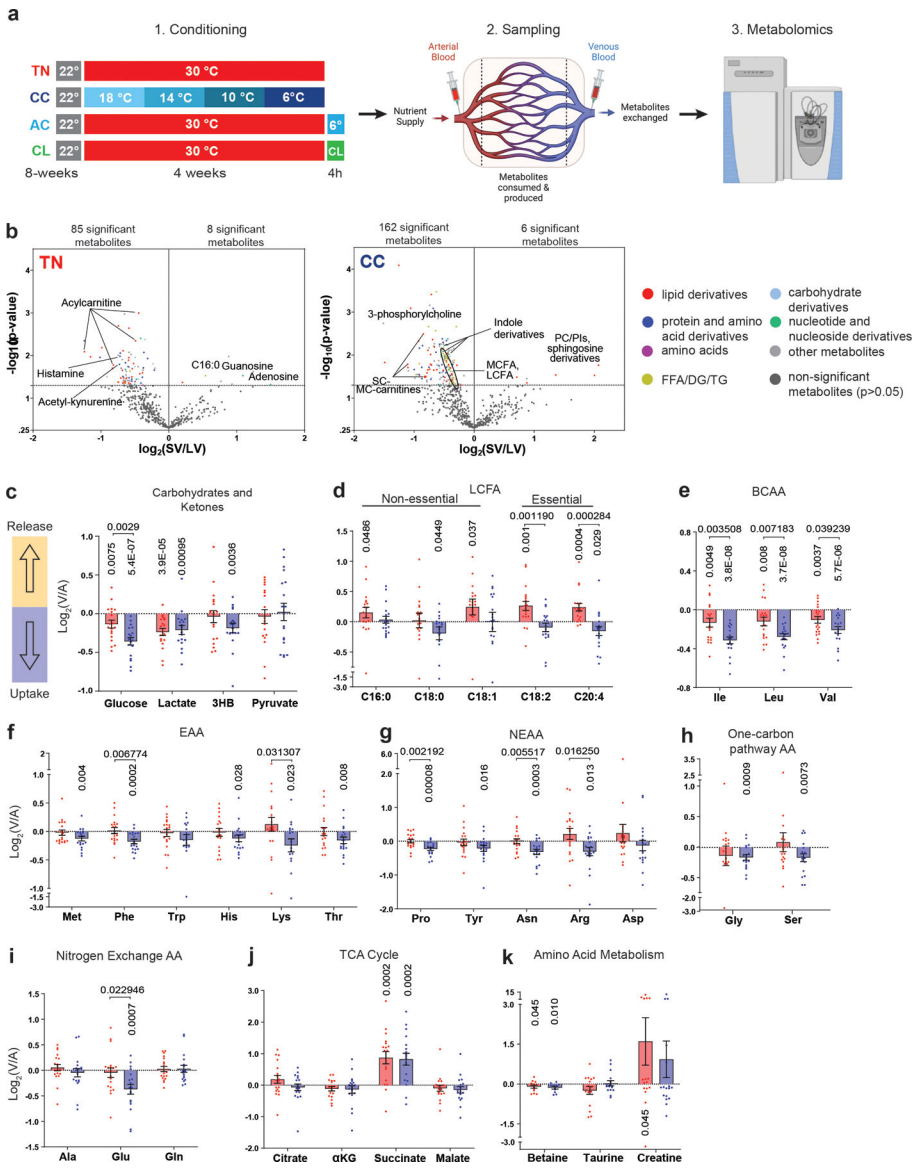

Fig. 1. Arterio-venous (AV) metabolomics reveals broadly altered metabolic activities of BAT in cold-adapted mice.

a, Experimental scheme of AV metabolomics under thermoneutral (TN), chronic cold (CC) adaptation, acute cold (AC) exposure, and CL-316,243 (CL) injection conditions. Made with BioRender.com. **b**, CC-adapted BAT absorbs a variety of circulating metabolites. Volcano plots show changes in BAT's metabolite uptake and release in TN and CC. Different colors indicate metabolite categories. MC, medium-chain; SC, short-chain; PC, phosphatidylcholine; PI, phosphatidylinositol. **c-k**, BAT's uptake and release of the 35 abundant and high flux-carrying circulating fuel metabolites, categorized by the indicated groups. The data shows $\log_2$ V/A ratios. Individual data points represent each mouse. N=19 mice for TN and N=18 mice for CC. Data are mean ± s.e. P-values (vertical) compared to a null value (zero exchange) by 1-tailed one sample t-test. P-values (horizontal) compared to TN by two-paired Student's t-test. LCFA, long-chain fatty acids, BCAA; branched-chain amino acids, EAA; essential amino acids, NEAA; non-essential amino acids.

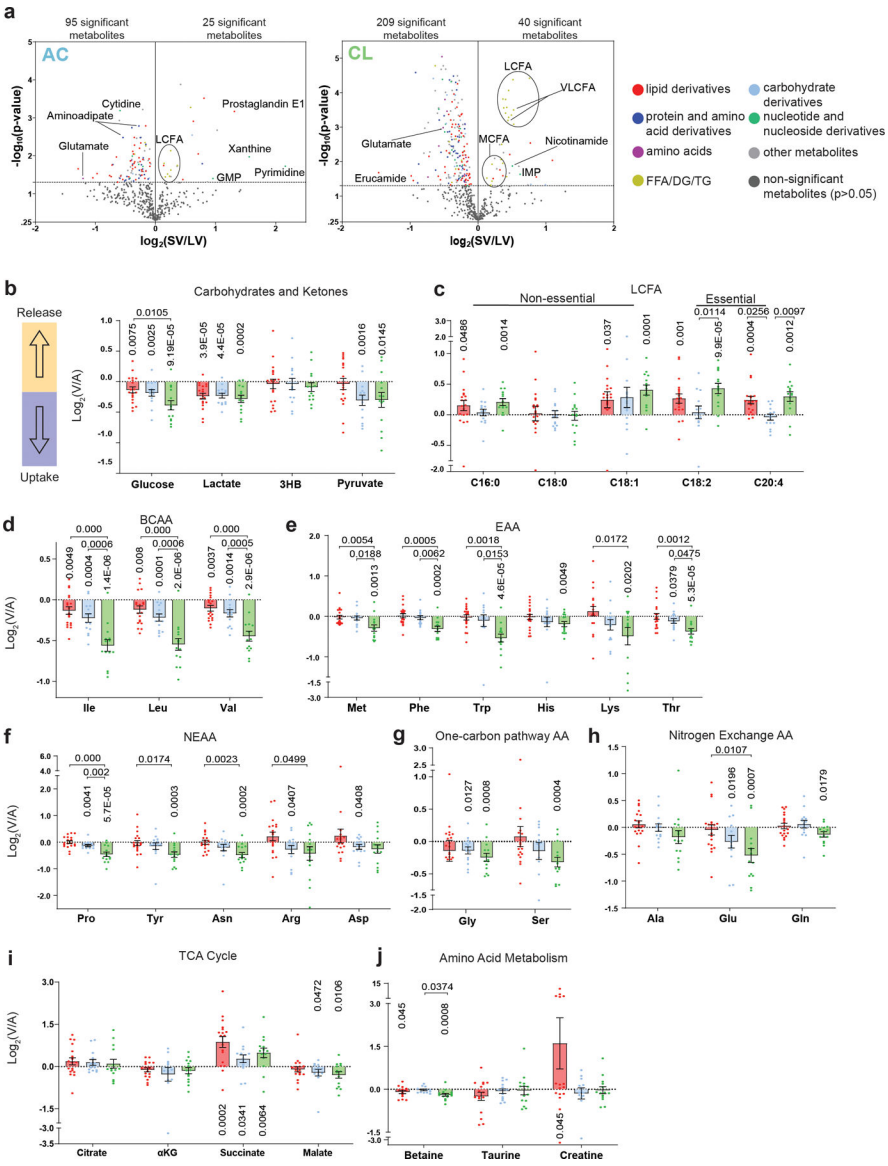

Fig 2. Acute cold challenge is only partially replicated by pharmacological β-adrenergic receptor activation.

a, Volcano plots show changes in BAT's metabolite uptake and release in AC and CL. Different colors indicate metabolite categories. **b-j**, BAT's uptake and release of the 35 abundant and high flux-carrying circulating fuel metabolites, categorized by the indicated groups. The data shows $\log_2$ V/A ratios. Individual data points represent each mouse. N=19 mice for TN and N=14 mice for AC and CL. Data are mean ± s.e. P-values (vertical) compared to null value (zero exchange) by 1-tailed one sample t-test. P-values (horizontal) for group differences determined via one-tailed ANOVA with Tukey's HSD.

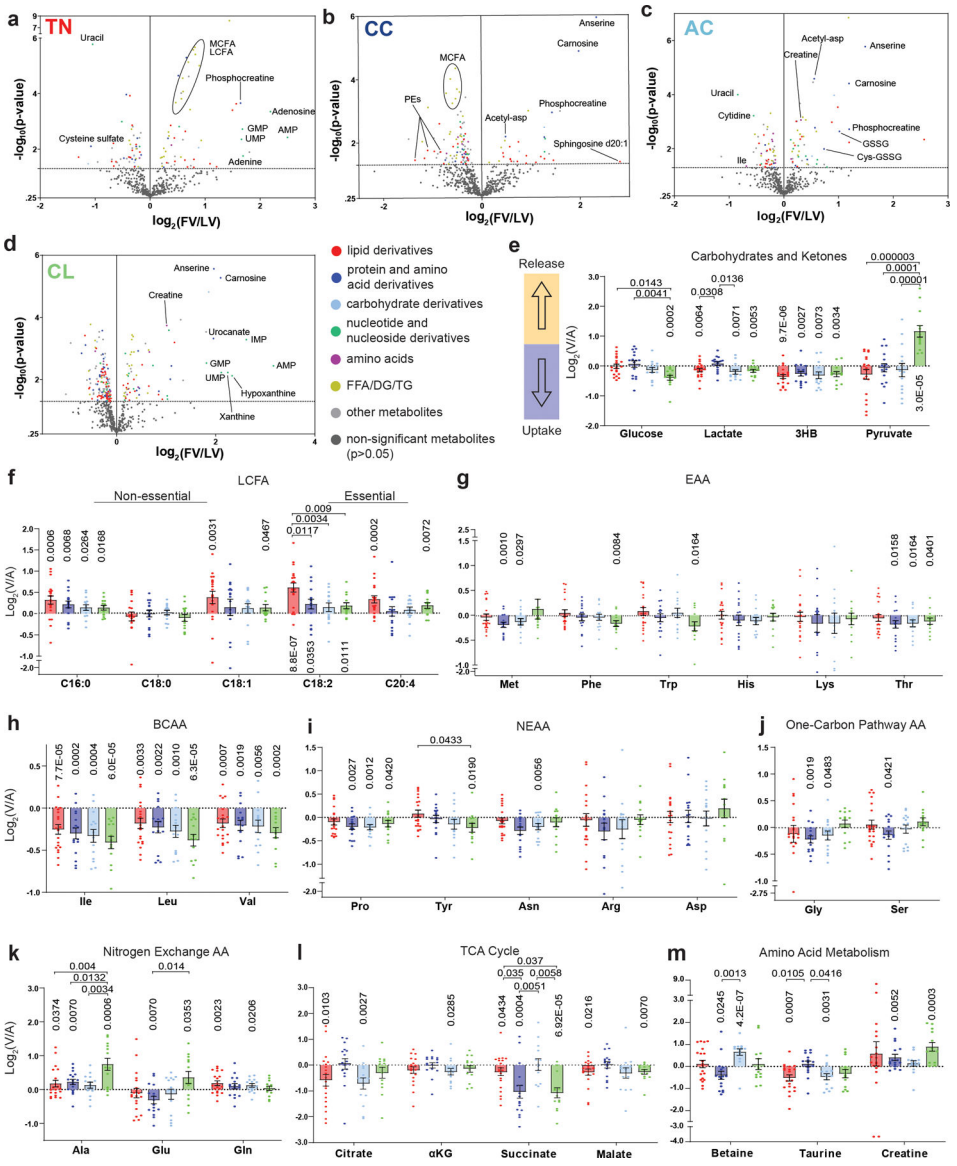

Fig. 3. The landscape of leg metabolic activities under various thermogenic conditions.

a-d, Volcano plots show changes in leg metabolite uptake and release across TN, CC, AC and CL conditions. Different colors indicate metabolite categories. PE, phosphatidylethanolamine; GSSG, glutathione disulfide. **e-m**, Leg uptake and release of the 35 abundant and high flux-carrying circulating fuel metabolites, categorized by the indicated groups. The data shows $\log_2$ V/A ratios. Individual data points represent each mouse. N=20 mice for TN, N=16 mice for CC, N=14 mice for AC, and N=13 mice for CL. Data are mean ± s.e. P-values (vertical) compared to a null value (zero exchange) by 1-tailed one sample t-test. P-values (horizontal) for group differences determined via one-tailed ANOVA with Tukey's HSD.

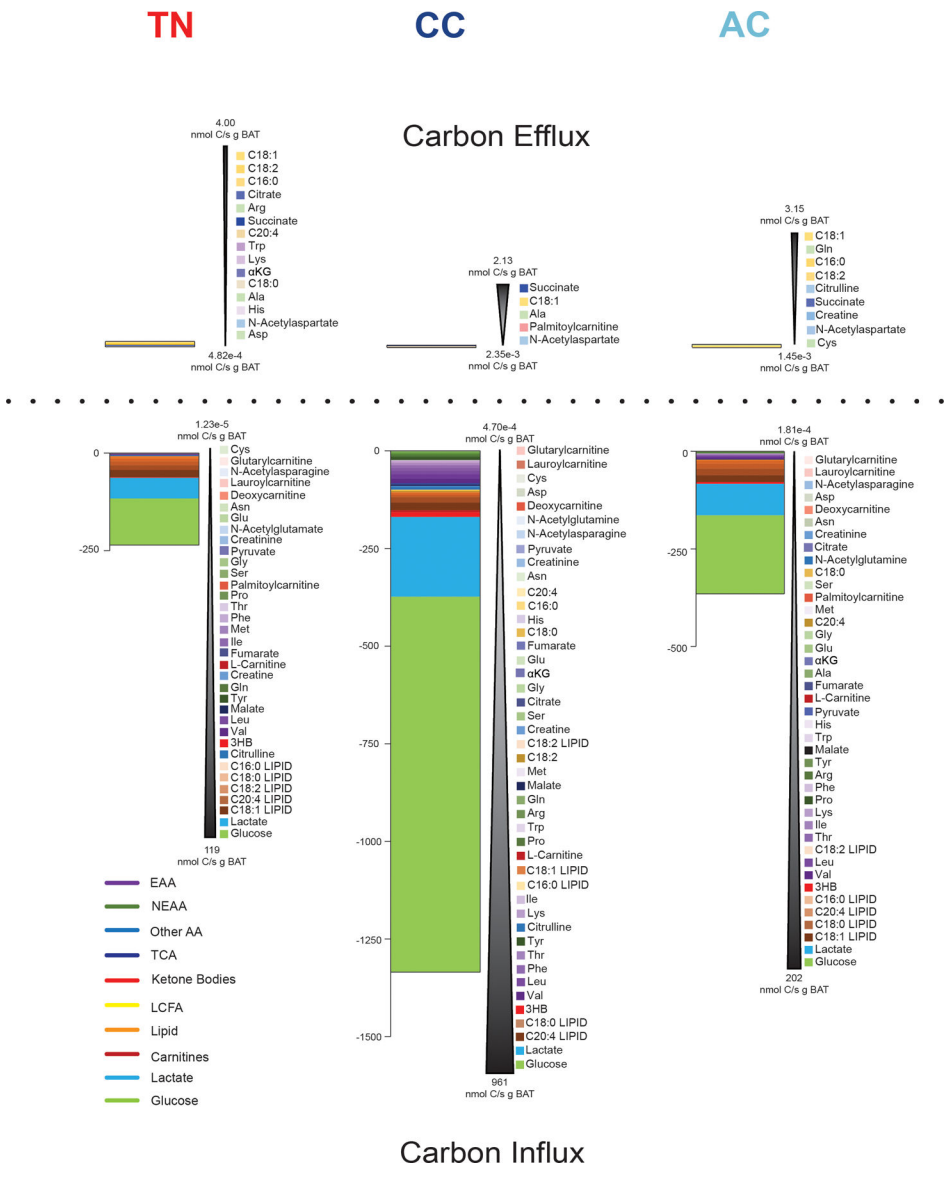

Fig 4. Quantitative analysis of BAT carbon influx and efflux.

Colors indicate different metabolite categories. Metabolites are ordered based on their relative contributions from greatest to least. Fatty acids from lipoprotein particles are indicated as “LIPID” after each fatty acid species (e.g., C16:0 LIPID).

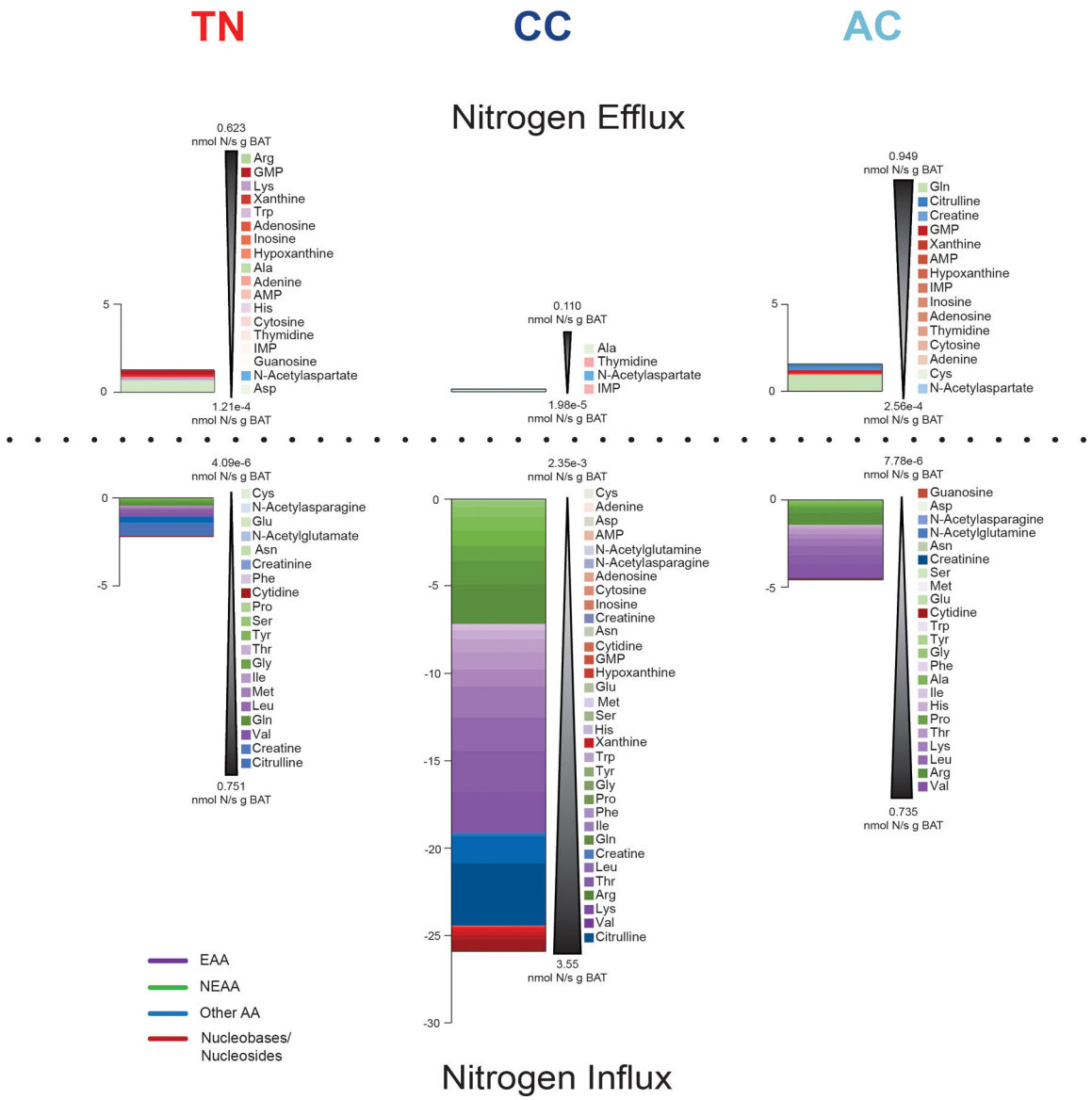

Fig 5. Quantitative analysis of BAT nitrogen influx and efflux.

Colors indicate different metabolite categories. Metabolites are ordered based on their relative contributions from greatest to least.

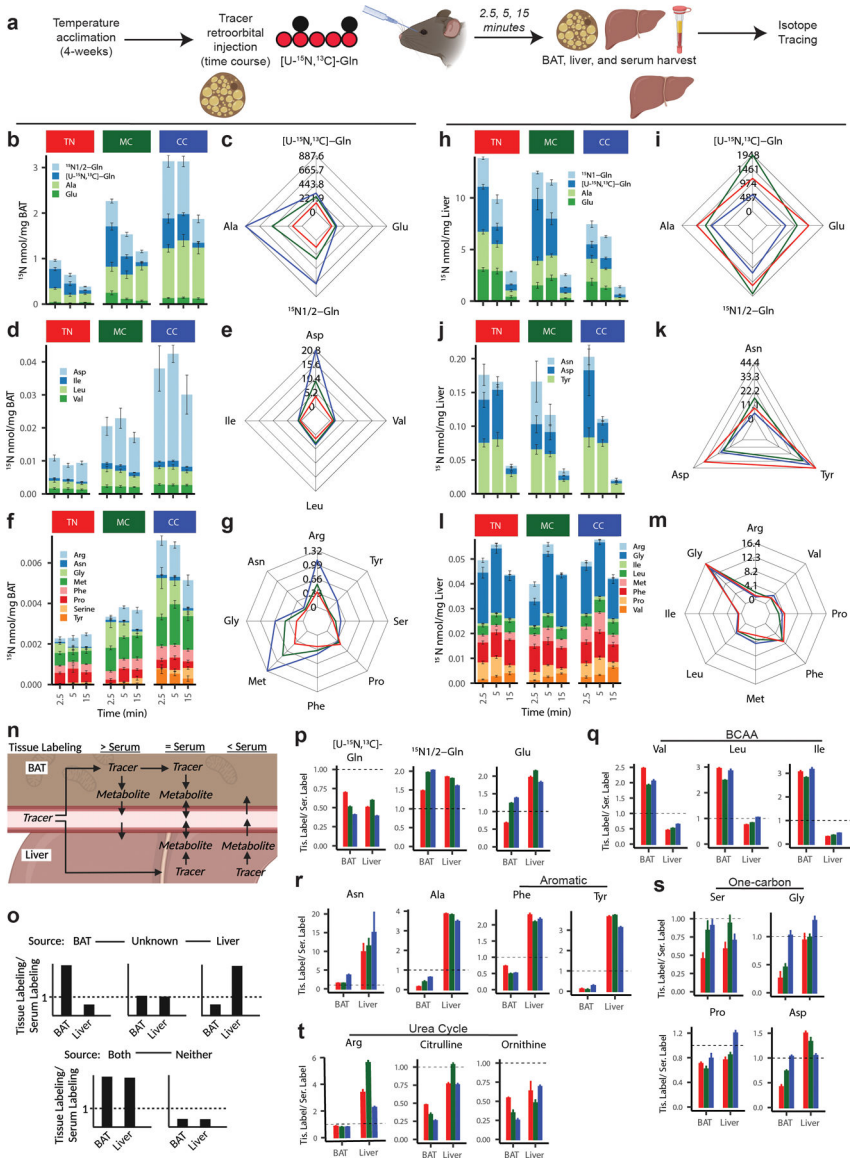

Fig. 6. Distinct usage of glutamine nitrogen by BAT and liver at different temperatures.

a, Schematic of in vivo glutamine tracing experiment. Made with BioRender.com. **b-m**, Various usage of glutamine nitrogen in BAT (**b-g**) versus liver (**h-m**) in TN, MC and CC. Bar graphs show the concentration of ^{15}N-labeled metabolites at each time point, with the most abundant metabolites shown on the top. Spider plots show area under-curve. N=6 mice for TN, N=6 mice for MC, N=7 mice CC at 2.5 min, N=6 mice for all temperature conditions at 5 min, N=6 mice for TN, N=6 mice for MC, N=5 mice for CC at 15 min. Data are mean ± s.e. **n**, Schematic depicting various scenarios of metabolite production from glutamine in BAT versus liver and their exchange via circulation. Made with BioRender.com. **o**, Comparison of fractional labeling between BAT, liver, and serum informs the production site of the labeled metabolites, with higher labeling in a certain tissue than blood reflecting its generation by the tissue. Made with BioRender.com. **p-t**, Means indicate 95% confidence interval for fold changes of average AUC of tissue fractional

labeling versus serum. Error bars indicate 95% CI calculated with bootstrapping utilizing 10,000 simulations. N=18 mice for TN, N=18 mice for MC, N=18 mice for CC.

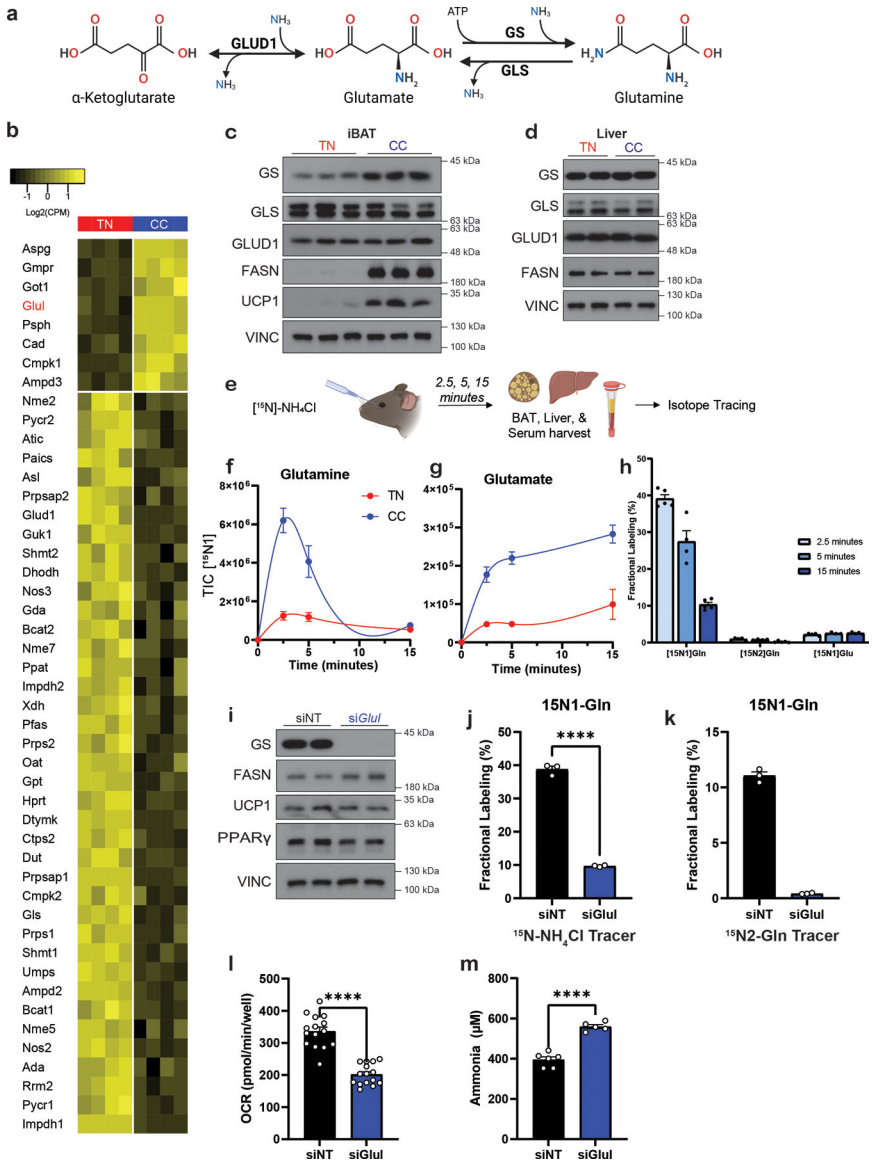

Fig. 7. Cold-induced glutamine synthetase facilitates fuel oxidation in BAT by scavenging ammonia.

a. Schematic of glutamine synthesis and catabolism. Made with BioRender.com. **b,** Heatmap of nitrogen metabolism genes with FDR values less than 3% scaled for each gene. **c-d,** Western blots show induction of GS in CC only in BAT (**c**) but not in liver (**d**). **e,** Schematic of in vivo ammonia tracing experiment. Made with BioRender.com. **f-h**, ^{15}N1-labeled glutamine (**f**) and glutamate (**g**) abundances in BAT from mice in TN versus CC and labeling fractions of ^{15}N-labeled Gln and Glu isotopomers in BAT from mice in CC (**h**). N=5 mice were used for each time point except TN 15-minute and CC 5-minute N=4 mice were used (**f-h**). Data are mean ± s.e. TIC, total ion count. **i**, Western blots show mature brown adipocytes transfected with siRNA non-target (siNT) or targeting *Glul* (si*Glul*). **j-k**, ^{15}N1-labeled glutamine fractional labeling after ^{15}N-NH_4Cl tracer (**j**) or ^{15}N2-Gln tracer (**k**) in mature brown adipocytes transfected with siNT or si*Glul*. Tracers were administered for 6 hours. N=3 biological replicates. Data are mean ± s.e. ****p=7×10^{-6} (**j**) and ****p=6×10^{-6}

(**k**) by unpaired two-tailed Student's t-test. **l**, Oxygen consumption rates (OCR) of mature brown adipocytes transfected with siNT or si*Glul*. N=15 biological replicates. Data are mean ± s.e. ****p=2×10^{-9} by unpaired two-tailed Student's t-test. **m**, Ammonia levels in the culture media of mature brown adipocytes transfected with siNT or si*Glul*. N=6 biological replicates. Data are mean ± s.e. ****p=8×10^{-6} by unpaired two-tailed Student's t-test.